Rapid Biofabrication of an Advanced Microphysiological System Mimicking Phenotypical Heterogeneity and Drug Resistance in Glioblastoma

Sirjana Pun, Anusha Prakash, Dalee Demaree, Daniel Pomeranz Krummel, Giuseppe Sciumè, Soma Sengupta, Riccardo Barrile

ADVANCED HEALTHCARE MATERIALS
www.advhealthmat.de

Rapid Biofabrication of an Advanced Microphysiological System Mimicking Phenotypical Heterogeneity and Drug Resistance in Glioblastoma

*Sirjana Pun, Anusha Prakash, Dalee Demaree, Daniel Pomeranz Krummel, Giuseppe Sciumè, Soma Sengupta, and Riccardo Barrile**

Microphysiological systems (MPSs) reconstitute tissue interfaces and organ functions, presenting a promising alternative to animal models in drug development. However, traditional materials like polydimethylsiloxane (PDMS) often interfere by absorbing hydrophobic molecules, affecting drug testing accuracy. Additive manufacturing, including 3D bioprinting, offers viable solutions. GlioFlow3D, a novel microfluidic platform combining extrusion bioprinting and stereolithography (SLA) is introduced. GlioFlow3D integrates primary human cells and glioblastoma (GBM) lines in hydrogel-based microchannels mimicking vasculature, within an SLA resin framework using cost-effective materials. The study introduces a robust protocol to mitigate SLA resin cytotoxicity. Compared to PDMS, GlioFlow3D demonstrated lower small molecule absorption, which is relevant for accurate testing of small molecules like Temozolomide (TMZ). Computational modeling is used to optimize a pumpless setup simulating interstitial fluid flow dynamics in tissues. Co-culturing GBM with brain endothelial cells in GlioFlow3D showed enhanced CD133 expression and TMZ resistance near vascular interfaces, highlighting spatial drug resistance mechanisms. This PDMS-free platform promises advanced drug testing, improving preclinical research and personalized therapy by elucidating complex GBM drug resistance mechanisms influenced by the tissue microenvironment.

1. Introduction

To date, animal models serve as the primary preclinical models for testing drug efficacy and toxicity. However, the physiological and anatomical differences between animals and humans contribute to drugs failing safety and efficacy criteria in clinical trials.[1,2] As awareness grows regarding the limitations of the traditional drug development pipeline, recent legislations, exemplified by the Food and Drug Administration (FDA) Modernization Act 2.0 in the USA,[3] have eliminated the mandatory requirement for animal testing of drugs and cosmetics. This underscores a crucial shift and emphasizes the growing demand for Microphysiological systems (MPSs) that more accurately reflect human biology.

MPSs, including engineered in vitro systems such as Organs-on-Chips (OoCs), represent a paradigm shift in preclinical research.[4] These models integrate diverse cell types within dynamic culture conditions, surpassing the limitations of traditional static cell culture

S. Pun, A. Prakash, D. Demaree, R. Barrile
Department of Biomedical Engineering
University of Cincinnati
Cincinnati, OH 45221, USA
E-mail: riccardo.barrile@uc.edu
A. Prakash
Abbvie
Worcester, Massachusetts 01605, USA
D. Demaree
Thermo Fisher Scientific
Waltham, Massachusetts 02451, USA
D. P. Krummel, S. Sengupta
Department of Neurology
University of Cincinnati
Cincinnati, OH 45219, USA
D. P. Krummel, S. Sengupta
Department of Neurosurgery
University of North Carolina
Chapel Hill, NC 27599, USA
G. Sciumè
Institute of Mechanics and Engineering-12 M
University of Bordeaux
Bordeaux 33607, France
S. Sengupta
Department of Neurology
University of North Carolina
Chapel Hill, NC 27599-7025, USA

The ORCID identification number(s) for the author(s) of this article can be found under https://doi.org/10.1002/adhm.202401876

DOI: 10.1002/adhm.202401876

methods. By recapitulating human tissue and organ function, MPSs offer a physiologically relevant environment that closely mimics the natural conditions of human tissues. This enables comprehensive studies of cell-cell interactions and the impacts of various compounds or treatments, providing invaluable insights into the effects of drugs and potential treatments.[4,5] Despite advancements supported by a growing body of proof-of-concept studies showcasing the translational potential and cost-effectiveness of these technologies,[6–11] their adoption in the pharmaceutical pipeline remains low. There are important limitations that must be addressed to bolster the robustness of these technologies for translational applications.[12,13]

Conventional methods for generating OoCs are rooted in electronic chip manufacturing, utilizing polydimethylsiloxane (PDMS) for fabrication, requiring access to specialized equipment, often within a clean room setting, and the involvement of highly specialized personnel hindering scalability and customization. Additionally, PDMS exhibits variable and time-dependent absorption of small, hydrophobic molecules.[14] This makes it potentially unsuitable for drug testing of small molecules, which account for the largest (>90%) class of therapeutics targeting the central nervous system.[15]

The increasing accessibility of 3D printing technologies has facilitated the fabrication of microfluidic hydrogels, an area often recognized as "soft microfluidics".[16,17] This trend is challenging the conventional PDMS-based systems, with bio-inspired materials progressively replacing traditional synthetic elastomers.[18] Extrusion 3D printing, incorporating materials like polylactic acid (PLC) and utilizing techniques such as Fused Deposition Modeling (FDM), has been explored both independently and in combination with bioprinting of hydrogels in various proof-of-concept studies. Lee et.al. utilized the FDM-PLC platform that integrates hydrogels loaded with various cell types to investigate and analyze liver function.[19] Macdonald et.al. examined the suitability of the FDM technique, employing molten plastic, concerning precision, size, and throughput.[20] Their assessment encompassed a comparative analysis with alternative fabrication methodologies for constructing microfluidic devices. Similarly, Morgan et.al. employed FDM printing techniques using alginate ink infused with dental stem cells, further highlighting the utilization of this approach for fabricating MPSs.[21] These studies have highlighted the potential of additive manufacturing methods in generating microfluidic synthetic tissues. However, previous research has primarily centered around the one-step fabrication concept, frequently entailing the 3D printing of PDMS scaffolds followed by extrusion bioprinting of cell-laden hydrogels. This approach prolongs the biofabrication of each device, impeding the scalability of production and hindering the testing of small therapeutic compounds.

In this study, we introduce an optimized approach for the rapid prototyping of a functional microfluidic model of a human brain vessel. This method capitalizes on the heightened prototyping capabilities of stereolithography (SLA), seamlessly integrating its rapidity with the precision and biocompatibility afforded by extrusion bioprinting. By doing so, our approach eliminates the need for intricate microfabrication protocols and the assembly of microfluidic devices based on PDMS. We demonstrated that this method allows for robust biofabrication of hydrogel-based microfluidic systems housing human brain microvascular endothelial cells (HBMECs) and glial cells within rigid microfluidic scaffold obtained via SLA. In contrast to state-of-the-art methodologies like PDMS-based soft-lithography and other models obtained via one-step bioprinting, our method offers a more accessible, rapid, and versatile process for the efficient creation of vascularized MPS. Specifically, our approach mitigates concerns related to the absorption of small molecules, including a standard-of-care chemotherapeutic for brain tumors, Temozolomide (TMZ). At the same time, it addresses potential cytotoxicity linked to SLA resins.[22] These unique features position our system as an ideal and reliable platform for drug testing, particularly in neuroscience-focused research. To assess the dynamic culture capabilities of our platform, we broadened our study to co-culture HBMECs, primary astrocytes, and the well-characterized U87 cell line derived from human glioblastoma multiforme (GBM), the most prevalent form of primary brain tumor.[23] The incorporation of porous microfluidic hydrogels into our device facilitated the recreation of tissue-relevant interstitial fluid flow (IFF) and intravascular pressure, thus establishing a more physiologically relevant microenvironment of the cerebrovascular tissue. Maintaining over 90% cell viability, the system showcased HBMECs forming a compact cell monolayer along the walls of the microfluidic hydrogel, essentially replicating the vascular wall of a blood vessel. We evaluated both the barrier function of the vascular wall and its responsiveness when exposed to the pro-inflammatory microenvironment produced by tumor cells co-cultured within the same platform. The recreated dynamic microenvironment efficiently guides GBM tumor cells into cancer stem cells, expressing tissue-relevant biomarkers and developing drug resistance, particularly within the perivascular space – a critical element in GBM tumorigenesis.[24] Our results also demonstrate the capability of this model, for the first time, to mimic the protective role of primary HBMECs forming the blood-brain barrier (BBB) and harboring glioblastoma stem cell (GSCs)-like cells within a specialized niche protected from circulating TMZ,[25] a mechanism of drug resistance that is overlooked in traditional culture systems.

In summary, the present work highlights the potential of our approach in generating complex in vitro models leveraging the inherent self-assembly capacity of human cells into perfusable 3D microtissues that exhibit tissue-level functionality. This stands as a promising avenue for gaining profound insights into intricate human pathologies that prove challenging to investigate through alternative models.

S. Sengupta
Lineberger Comprehensive Cancer Center
University of North Carolina
Chapel Hill, NC 27599-7295, USA
R. Barrile
Center for Stem Cells and Organoid Medicine (CuSTOM)
Cincinnati Children's Hospital Medical Center
Cincinnati, OH 45229, USA

2. Results

2.1. Integrating SLA 3D Printing and Extrusion Bioprinting for Advanced Microphysiological Systems

In the present study, we explored the possibility of generating a robust and scalable scaffold that serves as a functional interface, connecting hydrogel-based tissue constructs with rigid microfluidic components required to generate fluid flow. Our microfabrication strategy combines the power of SLA 3D printing and extrusion bioprinting to create a scalable and functional MPS platform designed for capturing the dynamic microenvironment of the perivascular space in the glioblastoma interface. The SLA 3D printing technology is used to generate a rigid scaffold incorporating two microfluidic inlets oriented vertically to facilitate cell seeding (**Figure** 1A). The overall outer dimension of the chip is 50 mm (length) by 30 mm (width) by 12 mm (height). The inlets are thoughtfully designed to make them compatible with standard Luer-lock connectors, ensuring ease of cell seeding and seamless connection to commercially available syringes and microfluidic connectors (Figure 1B). Moreover, the inlets are interfaced with a microfluidic hydrogel obtained via sequential bioprinting of sacrificial material (Pluronic) and casting of a cell-laden pre-gel solution as described in Figure 1C,D. The step-by-step approach for the removal of Pluronic and seeding of endothelial cells is illustrated in Figure S1 (Supporting Information). The entire system is designed to be transparent, and PDMS-free, allowing for conventional microscopic assays and high-resolution imaging. To further enhance the interaction between the hydrogel and the 3D-printed scaffold, we incorporated pillar structures along the inner surface of 3D-printed parts (Figure S2A, Supporting Information). These pillar structures serve to optimize the surface interactions, reinforcing the stability and integrity of the hydrogel within the microfluidic environment. A direct comparison with other 3D printing methods commonly employed for the fabrication of microfluidic constructs, such as the fusion of PLC with FDM or the extrusion-based fabrication of PDMS,[20,26–28] highlights the superiority of the combined SLA and bioprinting approach (Figure S2A–C, Supporting Information). In particular, the microfluidic construct generated via PLC-FDM resulted in the lowest resolution and was not able to generate the inlets lower than 1 mm. Also, the porous nature of the material presents a significant challenge in keeping the system sterile for cell culture. PDMS-extrusion exhibited superior resolution compared to PLC microfluidics. However, the extended printing time, often exceeding an hour for the fabrication of a single device, rendered it impractical for swift prototyping and customization. On the contrary, the combination of SLA and bioprinting proved to be a more efficient alternative, allowing for the rapid incorporation of cell-laden hydrogels in just a few minutes while delivering superior resolution. By harnessing the capabilities of both SLA and extrusion bioprinting, our microfabrication strategy offers a wide range of design possibilities with remarkable ease and efficiency as depicted in Figure 1E. This showcases the potential of the chip design to be adapted for different tissues, organs, and disease states. This synergy between SLA and bioprinting enables an unparalleled resolution, expeditious prototyping, and the realization of a finely crafted microfluidic architecture that seamlessly accommodates cell seeding and fluidic flow.

2.2. Synergistic SLA and Extrusion Bioprinting Enable Efficient Fabrication of Low-Absorption, Highly Biocompatible Microfluidic Constructs

This study aims to develop a robust protocol for adapting SLA resin for the biofabrication of cell culture devices. SLA resins, while recognized for their high precision, have garnered a reputation for poor compatibility with cell-culture applications. Prior studies have explored various approaches to mitigate the cytotoxic effects of SLA resins. Extending the UV-curing time, employing isopropanol washing, and subjecting the materials to elevated temperatures (above 60 °C) have shown some promise in reducing the leaching of uncured components.[22] However, the lack of a definitive consensus in the field highlights the need for more effective methods to ensure material biocompatibility and safety. We adopted a live imaging approach (live/dead assay) to assess the biocompatibility of the microfluidic SLA parts.[29] Our test consisted of multiple steps captured in **Figure** 2A. Briefly, the SLA parts made of Grey Resin (Formlabs) were first cleaned in isopropanol overnight, then rinsed in Hanks' Balanced Salt Solution (HBSS) and let dry at 70 °C overnight. To determine the optimal duration of isopropanol treatment, the SLA parts underwent isopropanol treatment for different time intervals: 30 min, 1 hr., 3 hrs., and overnight. At each time point, the SLA parts were rinsed in HBSS and then soaked in cell culture medium for 24 h to generate the conditioned medium later used to culture human endothelial cells. Our results indicate that isopropanol washing of 3 h or more (overnight) combined with extended heating time prevents cell death and improves the biocompatibility of the SLA resin (Figure 2B,C). Cells growing in conditioned medium obtained from SLA parts before any treatment (untreated) display clear signs of cytotoxicity while treatment with isopropanol reduced and completely suppressed the cytotoxicity effect of the SLA parts. The overnight treatment showed similar results as the control group indicating the effectiveness of isopropanol treatment in maintaining cell viability. To validate the biocompatibility of SLA parts when cells are cultured in close proximity to this material, we assessed the viability of multiple cell types all cultured within the microfluidic device. The device was fabricated through sequential bioprinting of sacrificial hydrogel, followed by the casting of a fibrin(ogen) pre-gel solution. The human-derived glioblastoma cell line U87 and primary astrocytes were housed within the fibrin gel while HBMECs were seeded within the microfluidic channel formed at the interface of the fibrin gel and the underlying glass slide at the base of the newly generated microfluidic construct. All 3 cell types remained viable for at least 8 days (Figure 2D,E). Based on these findings, we decided to proceed with the overnight treatment option for all subsequent experiments, as it proved to be the most favorable in terms of cell viability and compatibility with the SLA resin chips.

One of the biggest concerns using the traditional PDMS device is that it shows time-dependent absorption of small molecules which are the largest group of therapeutic molecules for treating neurovascular diseases.[14] This limitation hampers their suit-

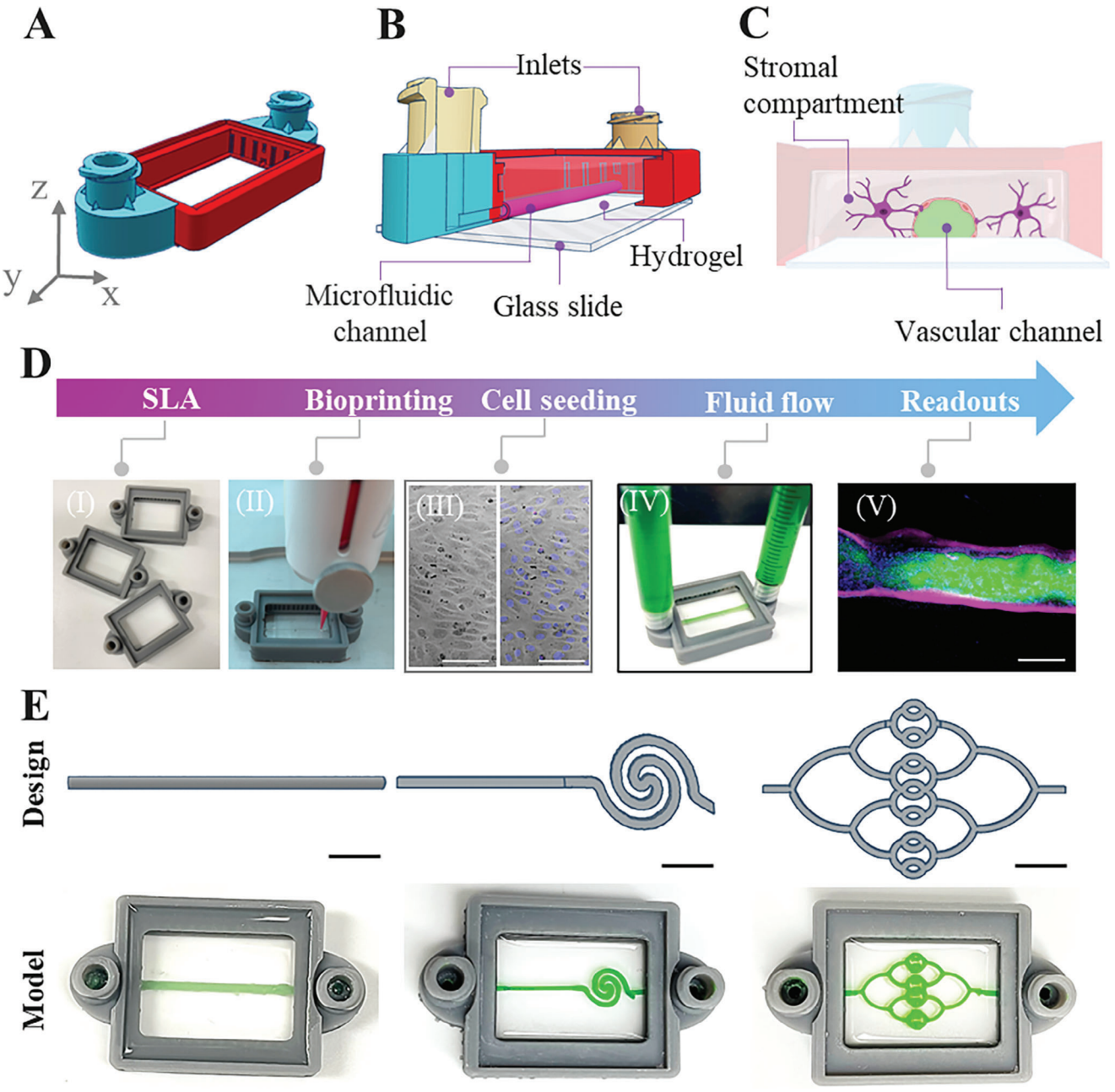

Figure 1. Schematics and Representative Images Illustrating the Assembly of a 3D-bioprinted System. A) 3D CAD design of the microfluidic scaffold. B) The 3D sectional view of the system highlights the microfluidic inlets, glass bottom, hydrogel compartment, and the vascular channel positioned on the glass surface. C) The stromal compartment comprising cancer cells and other glial cells such as astrocytes and a vascular compartment lined with brain endothelial cells are shown in the vertical cross-section. D) The microfabrication approach combines SLA and extrusion bioprinting methods. I) The microfluidic scaffold is designed using readily available software, 3D printed using a commercial SLA printer, and bound to a thin glass coverslip. II) Extrusion-based 3D bioprinting is used to print sacrificial material over the glass slide further covered with biocompatible hydrogels such as fibrin. Once polymerized, the sacrificial material is removed and the resulting microchannel is coated with a thin layer of extracellular matrix and seeded with HBMECs. III) Endothelial cells form a compact monolayer within 2–3 days post-cell seeding. Phase and fluorescence microscopy images of HBMECs cells seeded in the bioprinted microchannel. Images were taken 3 days post-seeding. The image on the Left is a bright field, Right is: Merge of all three channels. Bright-field (Gray); HOECHST (Blue); DraQ7 (Magenta). Scale bar 50 µm IV) The luer-lock fitting integrated into our design facilitates the connection to commercially available syringes used as reservoirs for cell culture medium. V) Live imaging methods can be used at any time to monitor cell viability or the integrity of the reconstituted vascular wall using biocompatible fluorescent molecules. Wheat germ agglutinin (WGA647, Magenta) stains the vascular wall; dextran (Green) is perfused through the channel. Nuclei are stained for HOESCT (Blue). The image shows a merge of all three colors. Scale bar 500 µm. E) 3D CAD design and printed devices with geometries with increasing geometrical complexities and resolution, printed using a combination of SLA and extrusion bioprinting approaches. Scale bar 5 mm.

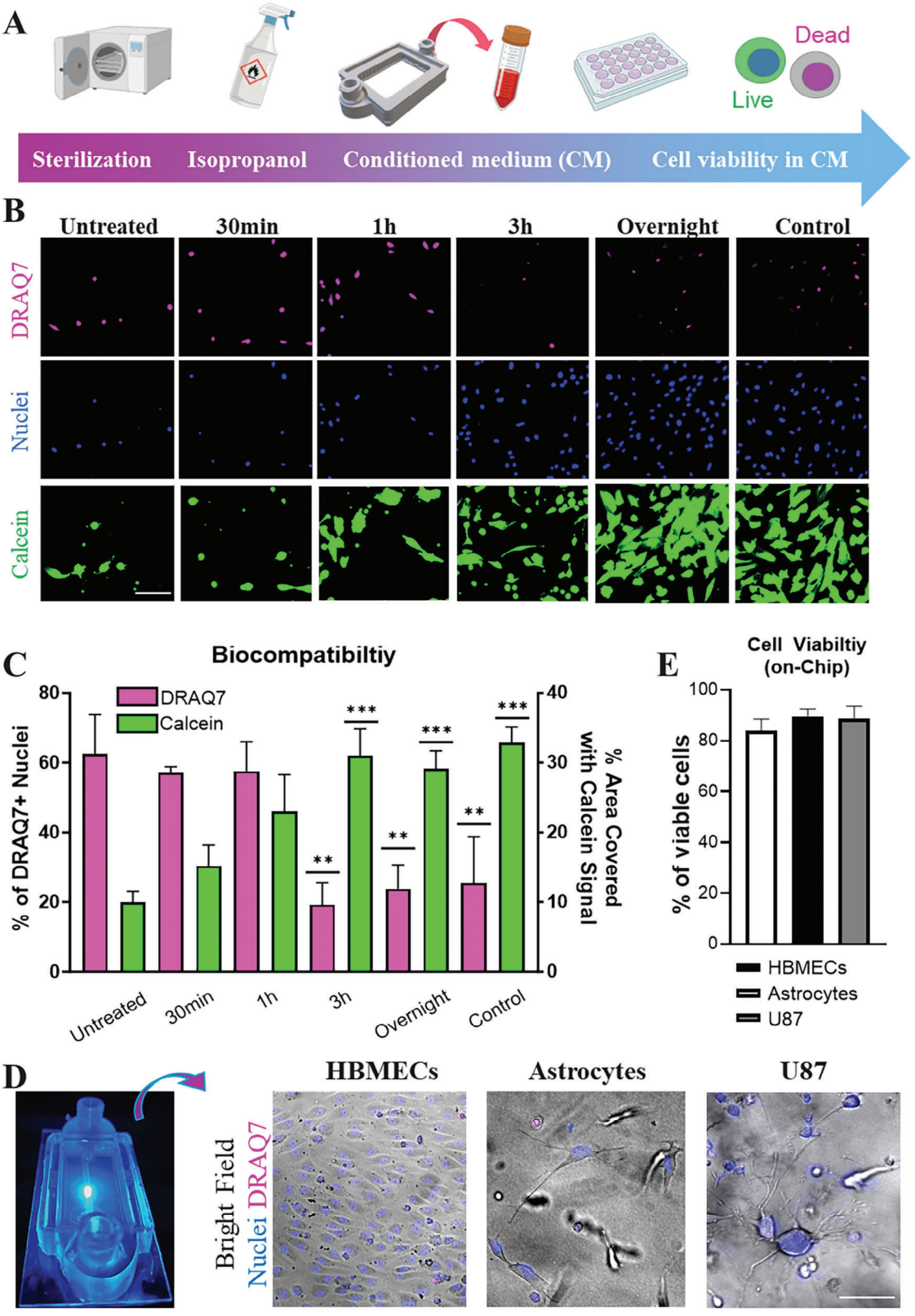

Figure 2. Biocompatibility Assessment of Newly Microfabricated Devices. A) The schematic shows the sequential experimental steps taken to assess the biocompatibility of 3D printed scaffolds after sterilization and isopropanol washing. B) Representative images obtained from a Live/dead assay used to evaluate the toxicity of 3D-printed resins used in this study. The 3D printed parts were soaked in isopropanol for various time points (30 min, 1 h, 3 h, and overnight). After treatment, the 3D printed parts were used to generate the conditioned medium later used to culture HBMECs for 3 days, as described in

ability for drug testing. To assess the absorption profile, PDMS was considered a reference material (**Figure 3**). Our investigation involved two small molecules: Rhodamine 123 (Rho123), a small (≈380 Da) fluorescent dye commonly used for assessing mitochondrial function and cellular activity and known to be absorbed by the PDMS[30]; TMZ a small (≈194 Da) lipophilic alkylating agent and standard of care in glioblastoma chemotherapy that is known for inducing DNA damage and cell death in rapidly dividing cancer cells.[31] We perfused our microfluidic scaffold with Rho123 and TMZ to evaluate their absorption profiles. Since our primary objective was to assess material absorption, we utilized only cell-free microfluidic scaffolds in this study. Initially, we evaluated the absorption properties of the 3D printed resin through fluorescence imaging of Rho123 as previously described by others.[30,32] Briefly, a Rho123 solution (1 µM in water) was injected into the microfluidic inlets and allowed to incubate overnight at room temperature. Subsequently, the excess Rho123 solution was removed, and the device was rinsed three times with water. Fluorescence microscopy was then used to capture residual fluorescence in the device inlets. Untreated devices were imaged to establish a baseline and rule out autofluorescence interference. The signal detected in the untreated devices was subtracted from that in the Rho123-perfused devices using ImageJ, and the results were reported as fluorescence intensity (graph in Figure 3A). Our findings revealed a higher level of Rho123 retention in the inlets of chips made of PDMS compared to those of our newly developed microfluidic device. Subsequently, we investigated the absorption properties of 3D printing resin and PDMS using a TMZ solution (12 mM in water). The solution was injected into the devices and allowed to incubate for ≈1 h. Subsequently, the solution was collected and analyzed via mass spectrometry to estimate the relative amount of TMZ absorbed by the two materials. Our results indicate that the relative amount of TMZ detected in the effluent of PDMS devices was extremely low (less than 5% of the initial concentration), suggesting that most (>90%) of the initial input was absorbed by the PDMS (Figure 3B). In contrast, the solution obtained after 1 h of incubation within the 3D printed scaffold obtained via SLA contained nearly the same amount as the initial input. These relative differences in concentration of the output reflect variations in the absorptive properties of the two materials. In summary, the result from both fluorescence imaging and mass spectrometry demonstrated that our newly microfabricated microfluidic device exhibited significant lower absorption of both Rho123 and TMZ when compared to traditional PDMS-based systems. This finding substantiates the benefits of our method in microfabricating a biocompatible microfluidic system that is amenable to small molecule testing. It presents a viable alternative to conventional PDMS-based approaches, particularly relevant for neurological applications where the use of small therapeutic compounds is much needed.

2.3. Leveraging Hydrogel-based Design for Mimicking Tissue Interstitial Fluid Flow

Hydrogels recapitulate multiple aspects of tissue physiology including porosity, permeability, and diffusivity. Given our ability to generate a biocompatible microfluidic construct, we have explored the opportunity to enhance and further generalize the current experimental setup and protocol to model physiological relevant biomechanical forces. Our study focused on two parameters, interstitial pressure and IFF which in *vivo* and in vitro are reported to be in the range of 0–4.5 µm $^{-1}$s.[33,34] To reconstitute a physiological pressure gradient that generates directional IFF between brain vessels and the parenchymal tissue in vivo, we modified our scaffold design by integrating reservoirs connected to the 3D printed inlets (**Figure** 4A,B). To induce a pressure-driven fluid flow across the gel, a pressure gradient between the vascular channel and the hydrogel is necessary. This gradient can be achieved by positioning a porous surface, such as a liquid-permeable membrane, on top of the hydrogel, effectively separating the hydrogel from the external environment at atmospheric pressure. Using an in-silico approach, we evaluated the impact of intravascular pressure and the permeability of the membrane on the IFF in the 3D bioprinted device. The hydrogel was treated as a porous medium with defined permeability and porosity.

For a given permeability and porosity of the gel,[35] by setting a pressure in the vessel of 500 Pa, the results depicted in Figure 4C,D show that the pressure profile along the orthogonal plane of the device varies for different permeability levels of the membrane. Results obtained via computational fluid dynamics also revealed a region characterized by high fluid velocity (IFF range 15–35 µm $^{-1}$s) near the perivascular space and a quasi-stagnant region at the periphery of the device (IFF range 0–5 µm $^{-1}$s) (Figure 4E), mimicking the in vivo conditions of a precapillary region in the brain. The in-silico model provided relevant insights for optimizing the design and parameters used to achieve physiologically relevant fluid dynamics in the 3D bioprinted device. To complement the computational results, we performed experiments to measure the IFF in vitro. The vertical reservoirs of devices bearing hydrogels, but no cells, were loaded with fluorescently labeled albumin (Albumin-Red, 250 ug mL^{-1}), used as a probe to measure the IFF generated when the medium in the microfluidic chamber was subjected to hydrostatic

detail in the experimental section/methods section. Cells cultured in nonconditioned media served as a control. At the end of the experiment, cells were stained with Calcein (green) and DRAQ7 (magenta) to detect live and dead cells, respectively. HOECHST (blue) was used for staining the cell nuclei. Scale bar: 50 µm. C) Numerical results from image analysis demonstrating the impact of isopropanol treatment on improving the biocompatibility of the SLA resin. Results are reported as percentages of DRAQ7+ and Calcein+ cells. The left y-axis of the graph shows the percentage of cell nuclei that stained positively for DRAQ7 in each field of view. The right y-axis shows the percentage of surface covered with Calcein signal in each field of view. Testing conditions are reported on the bottom (x-axis) of the graph and described in the results section of the manuscript. Ordinary one-way ANOVA was used to determine statistical significance denoted as $p > 0.05$ (ns), $0.01 < p < 0.05$ (*), $0.001 < p < 0.01$ (**), $0.0001 < p < 0.001$ (***), $n = 4$ biological replicates per condition, mean ± SEM. D) Fluorescence images of HBMECs, U87, and primary human astrocytes cultured within the 3D-printed model. Images were acquired 3 days post-coculture. DRAQ7 (Magenta); HOECHST (Blue); Bright field (Grey). Scale bar 50 µm. E) Numerical results of image analysis reporting the percentage of dead cells staining for DRAQ7+ after 5 days in culture on-chip. All the cell types maintain cell viability above 80% while cultured on the 3D-bioprinted model. Results are presented as mean ± SD, $n = 3$ biological replicates per condition.

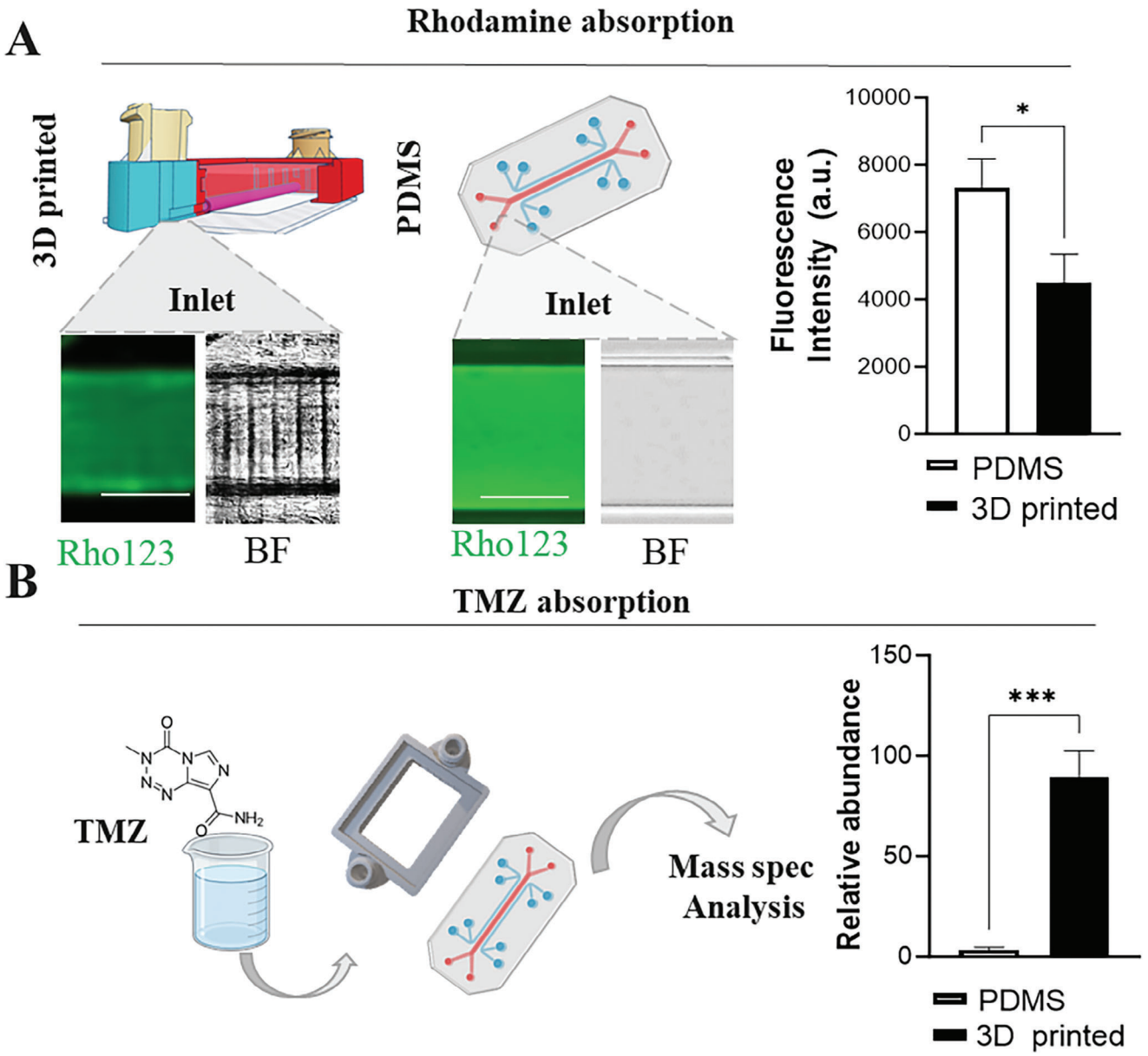

Figure 3. Small Molecule Absorption of a 3D-Printed Microfluidic Model Compared to Traditional PDMS. A) Microscopic images of the chip inlets showing the Rho123 signal retained by the two different materials. The Rho123 (380 Da) is visualized in green, while the bright field (BF) image is used to visualize the inlets of the 3D printed parts and in PDMS after overnight incubation with the dye and multiple rinsing steps. The graph on the right side of the figure reports the results of the image analysis performed on $n = 3$ devices confirming higher retention of Rho123 in PDMS. Scale bar 500 µm. An unpaired t-test was performed to determine statistical relevance. $0.01 < p < 0.05$ (*), $n = 3$, mean ± SD. B) TMZ (194 Da) was used as a tool molecular compound to determine the absorption properties of the 3D printed scaffold when compared to traditional PDMS Chips. The graph reports the results of mass spectrometry analysis performed in water collected from the effluent after 1 h of incubation. Results are reported as a percentage of TMZ in the effluent relative to the initial input. Unpaired t-test was performed to determine statistical significance denoted as $p > 0.05$ (ns), $0.01 < p < 0.05$ (*), $0.001 < p < 0.01$ (**), $0.0001 < p < 0.001$ (***). $n = 3$ devices, mean ± SD.

pressure in the inlets. To assess how fast the fluid flows from the microfluidic channel into the hydrogel under hydrostatic pressure, the region of the device comprised between the microfluidic channel and the 3D printed scaffold at the edge was monitored via continuous imaging and generation of large (≈5 mm) tiled images (Figure 4F). The measured average flow rate in the perivascular space (within 1 mm from the vascular wall) was 15 µm $^{-1}$s (Figure 4G). In the peripheral region of the device, the average flow rate was ≈5 µm $^{-1}$s. Overall, these results indicate that our modified scaffold design, incorporating a pressure gradient and a liquid-permeable membrane, can successfully mimic the directional IFF observed in vivo, thereby enhancing the physiological relevance of our 3D bioprinted model.

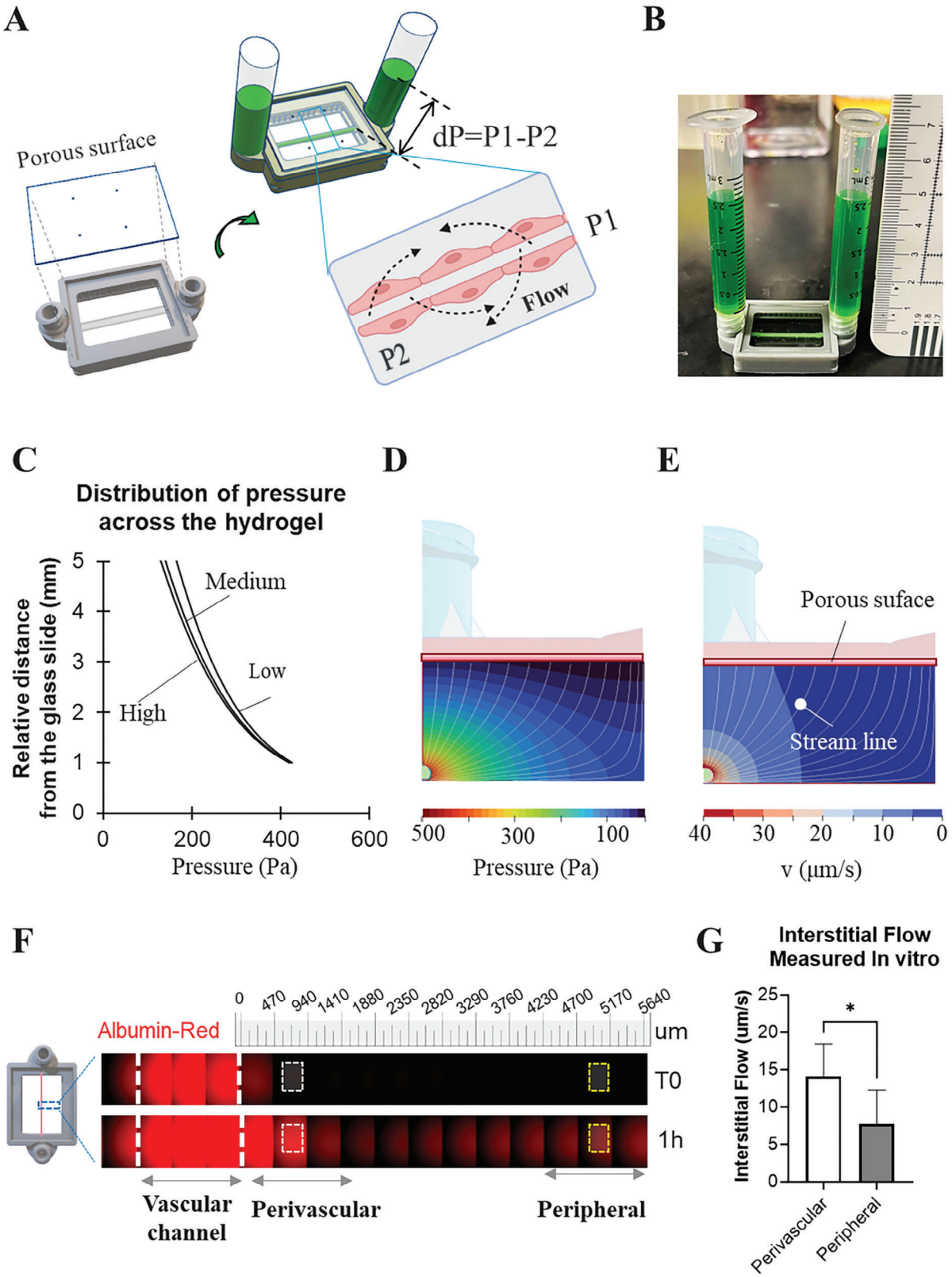

Figure 4. Recapitulating Physiologically Relevant IFF in a 3D Bioprinted Microenvironment. A) Schematic showing the concept of pressure-driven IFF from the vascular wall toward the hydrogel region. P1 represents intravascular pressure and P2 represents pressure in the extravascular region. B) Experimental setup to define intravascular pressure as 500 Pa higher than in the hydrogel region. Two reservoirs with a pressure head of 5 cm were placed in the inlets to generate the equivalent pressure of 500 Pa. To create the hydrostatic pressure difference, a liquid permeable membrane with

2.4. Recapitulating Loss of Vascular Barrier Function, and Secretion of Cytokines in a 3D Bioprinted Model of Glioblastoma

Given our demonstrated ability to biofabricating a microfluidic platform resembling physiological pressure and IFF, we next explored the possibility of adopting this newly developed platform for generating a functional vessel. To this end, HBMECs were seeded in the central channel of the microfluidic scaffold (**Figure 5**A). After 5 days in culture, we evaluated the condition of the endothelialized channel by perfusing a cell culture medium containing fluorescently labeled dextran as a fluid phase probe and fluorescently labeled wheat germ agglutinin (WGA647). This approach allowed simultaneous staining of the luminal surface of the endothelialized channel and to obtain visual confirmation of fluid flow (Figure 5B,C). After 6 days in culture, samples were fixed and stained to confirm the presence of key endothelial cell marker PECAM1 (Figure 5D). As anticipated, PECAM1 was localized within the perimeter of endothelial cells, demonstrating the establishment of a robust vascular wall lining the microfluidic hydrogel (Figure S3A,B,C, Movie S1, Supporting Information). Interesting findings emerged when the U87 cancer cell line replaced astrocytes, revealing a disjointed vascular wall (Figure 5E). The significant loss of vascular integrity was further corroborated via imaging of samples fixed at 2, 3, 4, and 5 days of co-culture. These images demonstrated a clear and progressive loss of vascular integrity, with the most pronounced deterioration observed within 5 days of coculture. (Figure S4A,B, Supporting Information). These results demonstrate that co-culturing with tumoral cells in this biofabricated system leads to significant damage to the vascular wall, a phenomenon believed to be a major contributor to cerebrovascular edema observed in GBM patients.[36,37] The hypothesis of an edema phenotype induced by GBM cells gained further support from previous in vivo studies involving U87 cells.[38] To provide functional evidence of an effective modulation of vascular leakage, we performed a barrier-function assay. Devices cultured only with HBMECs and co-cultured with healthy astrocytes or cancer U87 cells were used to assess the functionality of the micro-engineered vascular wall. After 5 days of co-culture, the vascular channel of the devices was perfused with fluorescent dextran (3 kDa). The amount of dextran diffusing outside of the vascular lumen into the parenchymal space was measured and reported as the coefficient of apparent permeability (pApp in Figure 5F,G). The results obtained from the barrier-function assay corroborated previous findings,[39] indicating that co-culturing with human astrocytes enhances the barrier function of the vascular wall. Conversely, the presence of brain tumor cells led to a loss of barrier function, simulating a condition reminiscent of edema which is further supported by the presence of pro-inflammatory molecules found in the medium obtained from devices cultured with U87 (Figure 5H). Upregulation of these cytokines in GBM has been reported in previous studies.[40] Moreover, the anticipated upregulation of MMP2, MMP9, and MMP12 expression, as evidenced in previous research,[41] supports the hypothesis that cancer cells can remodel the extracellular matrix (ECM) and migrate in our newly developed model (Figure 5I). In summary, our results confirm that the vascular wall of our bioengineered blood vessel presents barrier-function properties that can be modulated by the presence of the other brain cells simulating the physiological contribution of astrocytes and the detrimental effect of tumors on tissue microenvironment.

2.5. Dynamic Co-Culture Conditions Enhance Cancer Cell Differentiation in 2 Morphologically Distinct Populations

Microscopic analysis of microfluidic devices incorporating the GBM cell line U87 revealed the presence of two populations of cancer cells with distinct morphologies. Cells with a round morphology were located near the perivascular space of the device, while cells with a branched morphology were observed within the peripheral space (**Figure 6**A,B). Notably, the dynamic co-culture significantly enhanced the population of round cells in the perivascular space, whereas cancer cells growing in 3D fibrin hydrogel in traditional cell culture plates displayed a homogeneously branched morphology (Figure 6C). The distribution of each cell in a field of view is shown in the graph (Figure 6D). Our results demonstrate a statistically significant difference in the distribution of the two distinct cell morphologies between the perivascular space and the peripheral region of the device when cells were co-cultured under controlled fluid flow. Taken together, these results indicate that this phenotypical heterogeneity results from the self-arranging ability of cancer cells to reconstitute specialized niches, including the perivascular niche of brain tumors, similar to what occurs when these cells are transplanted into the brain tissue of living animals.[42,43] Encouraged by these promising outcomes, we embarked on further characterization of this system and exploration to highlight the platform's potential for constructing a vascularized model of GBM, subsequently named GlioFlow3D to differentiate this system from PDMS-based models obtained via traditional soft-lithography methods.

4 holes of diameter equal to 0.5 mm was used. C) The pressure curve shows the pressure distribution across the height of the gel corresponding to the permeability level of the membrane. Labels "low," "medium," and "high" represent the permeability levels of the top membrane. D) Pressure streamlines plot showing pressure distribution across the perivascular and peripheral regions. A vascular pressure of 500 Pa was applied in the channel. (E) Flow streamlines plot showing IFF in the perivascular and peripheral regions. Computer flow simulations estimated an IFF of 15–35 $\mu m^{-1}s$ in the perivascular region, while it was less than 0–5 $\mu m^{-1}s$ in the peripheral region. F) Empirical measurements were conducted in devices without cells to estimate interstitial flow in the experimental setup. Devices filled with fluorescent albumin (Albumin-Red) were imaged under fluorescent microscopy for 1 h. Fluorescent intensity measurements were taken immediately (T0) after injecting Albumin-Red (250 ug mL^{-1}) and again 1 h later (1 h). Multiple regions of interest (ROIs) were detected near the perivascular (white rectangles) and the peripheral (yellow rectangles) regions of the device. Images were processed as described in the materials and methods section under "Vascular Permeability". G) The measured average flow rate in the perivascular space (within 1 mm from the vascular wall) was 15 $\mu m^{-1}s$. In the peripheral region of the device, the average flow rate was ≈5 $\mu m^{-1}s$. Data obtained from $n = 3$ devices, mean ± SD. Unpaired t-test was performed to determine statistical significance denoted as $p > 0.05$ (ns), $0.01 < p < 0.05$ (*).

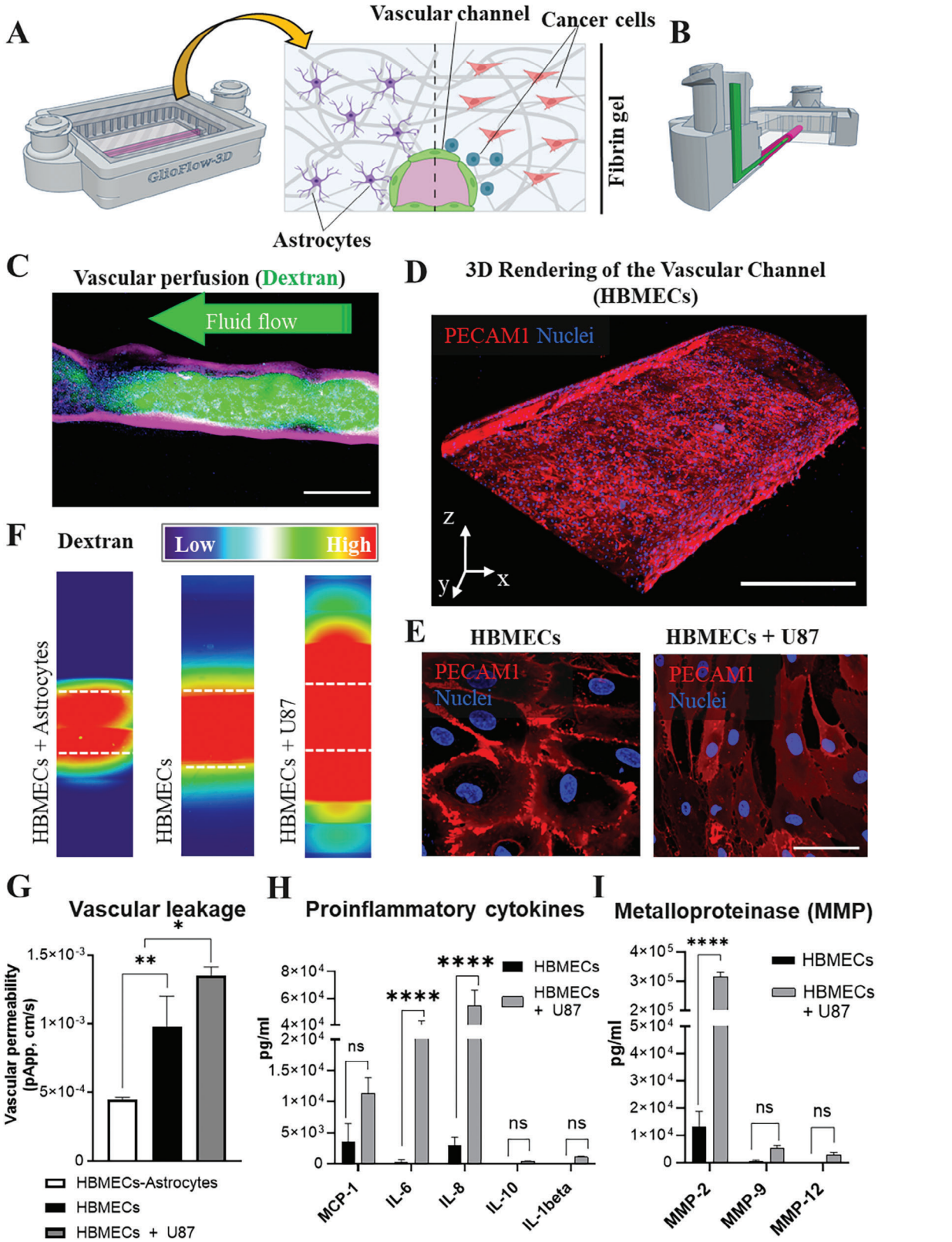

Figure 5. Capturing Vascular Dysfunction Caused by Glioblastoma in a 3D bioprinted Model of the Human BBB. A) Representative image of the SLA/bioprinted system. The microfluidic channel is highlighted in magenta. The cross-sectional image shows healthy tissue comprising of vascular channel and astrocytes (left half) and GBM tissue comprising of cancer cells and vascular channel. B) Cross-sectional diagram indicating fluorescent dextran (Green) flow through the inlet into the endothelialized microchannel (Magenta). C) Fluorescence image of live samples showing Dextran (Green)

2.6. The Glioflow3D Enables the Gaining of Spatial Information During Cancer Cell Progression and Drug Treatment

Similarly, to healthy tissues, brain tumors including GBM relies on the ability of a specialized cell subpopulation equipped with self-renewal potential named GSCs often found in peculiar regions (niches) of the brain.[44,45] GSCs characterized by a circular morphology and expressing CD133 are frequently found along vessels of experimental animals and clinical samples.[46–48] The relevance of studying this peculiar population of GSCs is highlighted by a growing body of evidence indicating a key role of these cells in initiating tumor regeneration and propagation after chemotherapy making these cells an important player during GBM recurrences.[49–52] Given the relevance of GSCs in tumor progression and drug resistance, we aimed to investigate whether the appearance of cells with a round morphology near the perivascular space correlates with an increase in CD133-positive cells in this region of the GlioFlow3D system. Samples cultured for 5 days under dynamic co-culture conditions were fixed and stained with the CD133 marker. Our results confirm the presence of round cells expressing CD133 in close proximity to the perivascular space (Figure 6E). In comparison, the branched cells situated in the outer region of the GlioFlow3D model exhibit a significantly reduced expression of CD133 (Figure 6F). This pattern mirrors the behavior of cancer cells cultivated in 3D fibrin gels under static conditions, highlighting a clear association between IFF in proximity to the perivascular space and an elevated expression of CD133 (Figure S5, Supporting Information). Our findings lead us to the conclusion that conventional static 3D cell culture techniques alone are inadequate to sustain the expression of CD133. However, under dynamic co-culture conditions, there is notable support for the expression of the CD133 marker in tumor cells situated in close proximity to the vascular space. Our conclusions are further corroborated by previous studies demonstrating that GSCs CD133+ are typically lost in traditional cell culture conditions.[53–55] This implies that the co-culture conditions implemented in the GlioFlow3D model recapitulate the essential conditions needed to drive the self-assembly of cells into the perivascular niche. Next, we explore the possibility that the perivascular niche acts as a shelter for tumor cells during chemotherapy, aiming to understand its protective role. We cultured cells in dynamic conditions in multiple GlioFlow3D systems for 2 days until reaching full confluency, as depicted in the schematic in **Figure** 7A. On the third day, the vascular compartment was perfused with a cell culture medium containing TMZ at a concentration of 12 mM, corresponding to the IC50 for these cells in 2D (Figure S6, Supporting Information). To ensure a constant supply of TMZ, all devices were connected to a microfluidic syringe pump as specified in the Materials and Methods section. After 3 days of continuous treatment, cell viability was assessed in both control and treated groups using an image-based approach. HOECHST served as a live stain for detecting all cell nuclei, while DRAQ7 selectively stained dead cells. Our findings revealed a significant impact of TMZ on the viability of cancer cells with a ramified morphology in the peripheral region of the GlioFlow3D (Figure 7B,C). Intriguingly, the percentage of dead cells in the periphery of the GlioFlow3D system mirrored that of cells growing in fibrin hydrogels on plates, indicating a similar sensitivity to the drug treatment. In contrast, cells in the perivascular region demonstrated higher resistance, as a significantly lower percentage of cells stained positive with the DRAQ7 in this region of the device. Taken together, these results demonstrate the possibility of using the GlioFlow3D to harness the inherent potential of human cancer cells to respond to the surrounding microenvironment and self-arrange into complex 3D structures that reflect the heterogeneous phenotype of GBM and the protective role of the perivascular space observed in vivo.

3. Discussion

The paradigm of MPS fabrication is currently experiencing a transformative shift, as researchers explore alternatives to classic fabrication methods and materials and a growing number of groups have been exploring the potential use of additive manufacturing methods to enhance microfabrication efficacy and reproducibility.[56,57] Bioprinting has recently emerged as a possible alternative to traditional microfabrication methods to generate advanced in vitro models for drug testing that include microfluidic hydrogels which better recapitulate the biochemical and biomechanical parameters of living tissues.[58] Lewis and colleagues pioneered this space via biofabricating microfluidic hydrogel models of the kidney framed within PDMS-based support with an elegant one-step approach.[59] Similarly, Lee et al. successfully generated a 3D-printed model of the liver using PLC as a rigid scaffold, printed with FDM technology.[19] While these studies demonstrated high cell viability due to the biocompatibility of PDMS and PLC, there are significant limitations that

flowing through the vascular channel, cells stained with WGA (Magenta) and HOECHST (Blue). Scale bar 500 µm. D) 3D rendering of the endothelial channel in HBMECs cultured for 6 days on-Chip and stained for PECAM1 (Red) and nuclei (Blue). Scale bar 500 µm. E) Confocal images of HBMECs cultured alone or with human cancer cells (U87) for 6 days and stained for PECAM1 (Red) and nuclei (Blue). Scale bar 25 µm. F) Representative images obtained during measurements of vascular permeability to estimate the barrier function of the vascular wall. These images illustrate vascular leakage of dextran through the endothelial wall, with lines indicating the endothelial wall. Images color-coded (Thermal map, red high concentration, blue low concentration of dextran). G) Vascular leakage reported as vascular permeability of dextran (3 kDa) across different culture conditions confirming the modulatory role of healthy astrocytes and tumor cells on the vascular wall of the HBMECs; Astrocytes strengthen the vascular wall function, reducing leakage, while cancer cells disrupt the barrier, increasing leakage. Data represents measurements obtained from $n = 3$–4 biological replicates per condition, mean ± SD. Two-way ANOVA test was used to determine statistical significance denoted as * ($0.01 < p < 0.05$), ** ($0.001 < p < 0.01$). (H) Quantitation of soluble proinflammatory cytokines detected in the medium of $n = 3$ biological replicates from both healthy and co-culture with cancer cells, measured using pre-labeled Luminex kits and expressed as mean ± SD. Two-way ANOVA was used to determine the statistical significance denoted as ns ($p > 0.05$), **** ($p < 0.0001$). (I) Quantitation of soluble metalloproteinase detected in the medium of $n \geq 3$ biological replicates from both healthy and co-culture with cancer cells, cultured for 6 days, measured using pre-labeled Luminex kits and expressed as mean ± SD. Two-way ANOVA was used to determine statistical significance denoted as ns ($p > 0.05$), **** ($p < 0.0001$).

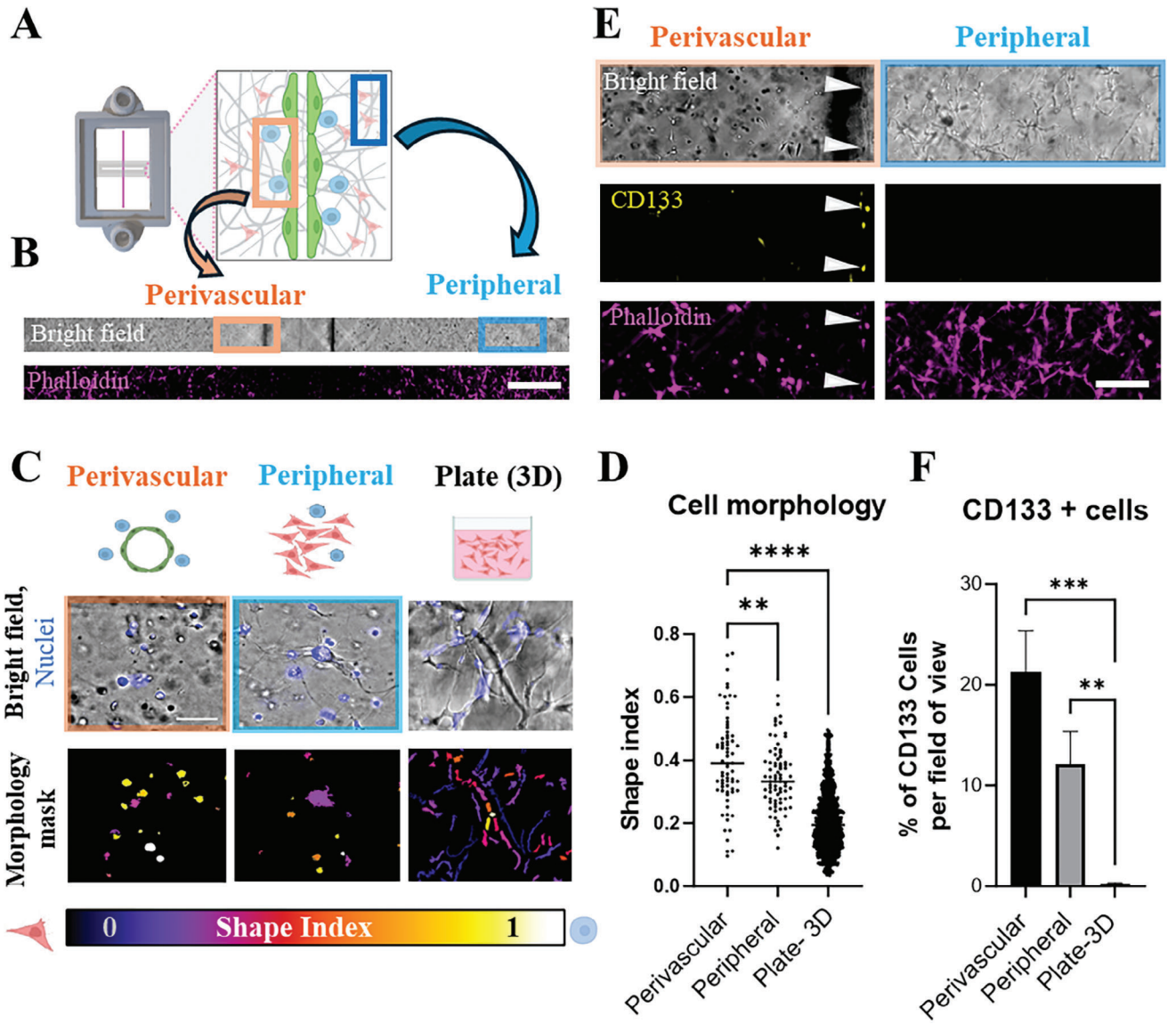

Figure 6. GlioFlow3D Recapitulates Phenotypical Tumor Heterogeneity. A) The schematic shows the top view of GlioFlow3D showcasing the heterogeneous cancer cell populations. B) The corresponding tile images showing bright field image (Grey) and Phalloidin (Magenta). Scale bar 500 µm. C) Glioblastoma U87 cells exhibit a round phenotype near endothelial cells (Perivascular) of the GlioFlow3D, contrasting with a branched phenotype in the region away from endothelial cells (Peripheral). Morphological differences are highlighted in bright field images (Gray), with nuclei stained by HOECHST (Blue). A morphology mask obtained from the processed bright field image emphasizes the prominent presence of round (circular) cells with shape index ≈1 in the perivascular space. Scale bar 50 µm. D) The graph shows the distribution of cells based on their shape. A cell shape index of 0 represents a branched phenotype, while an index of 1 represents perfectly circular cells. Each dot in the scattered plot represents a single cell. Ordinary one-way ANOVA tests was performed to determine statistical significance in respect to the perivascular space and denoted as ** ($0.001 < p < 0.01$) and *** ($0.0001 < p < 0.001$). Data were obtained from $n = 3$ biological replicates per condition. (E) Fluorescence microscopy images show differential expression of the self-renewal marker CD133 (Yellow) in cells within the perivascular and peripheral spaces of the GlioFlow3D device compared to static 3D hydrogels (Plate 3D). Cells are counter-stained with phalloidin (Magenta). The images shown are the zoomed-out images of the tile images present on the left side of the figure. Scale bar 100 µm. (F) Signal analysis for CD133 reveals a significant increase in expression in the perivascular space of the GlioFlow3D. Percentage of CD133+ cells were calculated in terms of nuclei. Results were obtained from image analysis (as described in the material and method section) of $n = 6$ biological replicates from 2 independent experiments and are expressed as mean ± SD. Ordinary one-way ANOVA test determines statistical significance denoted as ns ($p > 0.05$), * ($0.01 < p < 0.05$), ** ($0.001 < p < 0.01$), *** ($0.0001 < p < 0.001$).

hinder the widespread adoption of these technologies beyond specialized laboratories. PLC, for example, is extremely breakable and lacks transparency, limiting its utility for certain applications. Additionally, using PDMS as a conventional scaffold material for OoCs models presents challenges for drug testing, particularly with small molecules. The lengthy extrusion time required for fabricating these devices using the one-step approach further impedes the scaling up of these designs. Despite recent strides in the field, current approaches, including those utilizing shared source codes (G-Code), grapple with significant

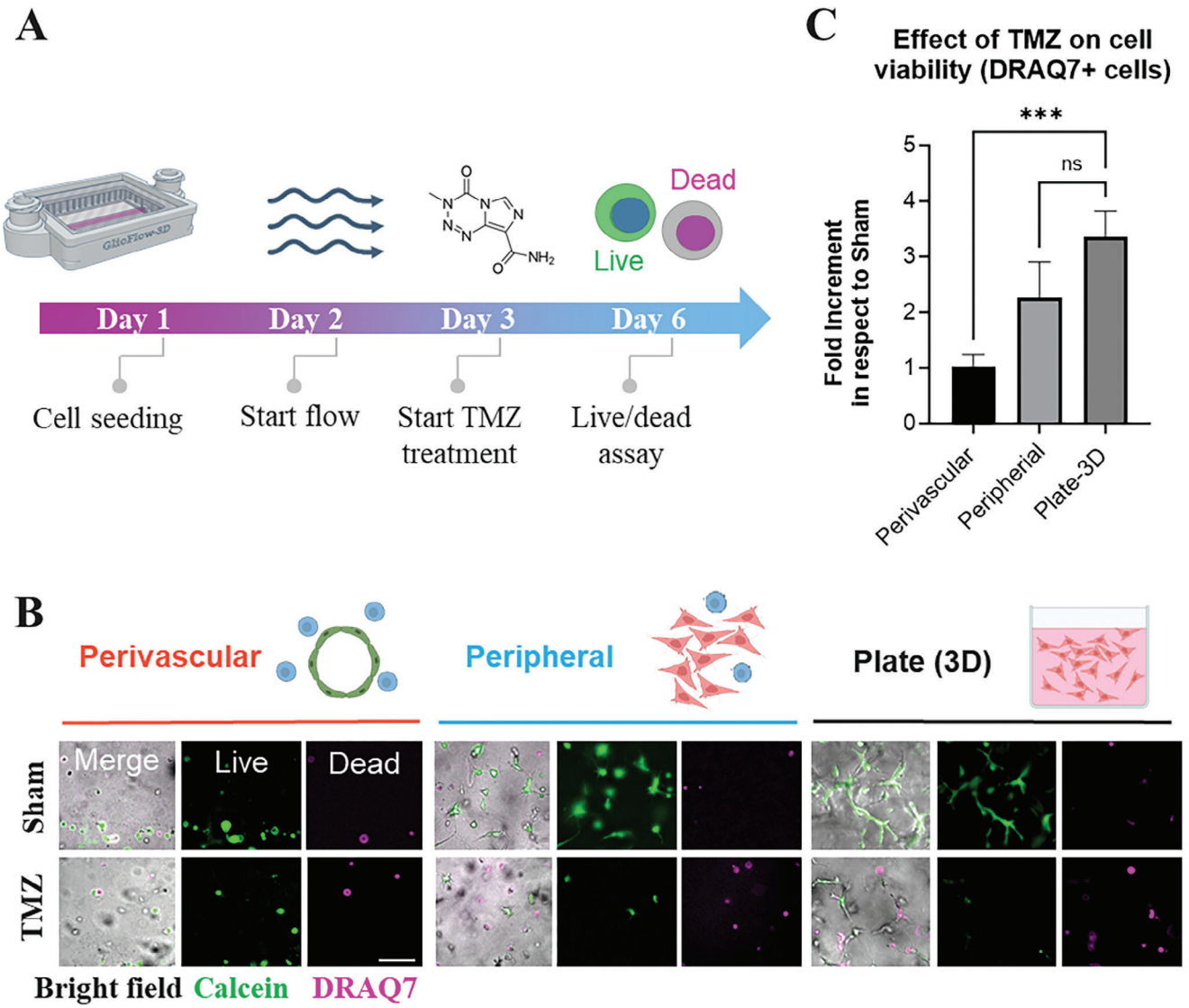

Figure 7. Glioblastoma Tumor Cells Within Perivascular Space Present Increased Drug Resistance to TMZ. A) Schematic illustrating the timeline of TMZ treatment for GBM cells. The GlioFlow3D was cultured under constant fluid flow for 2 days. TMZ was then injected into the vascular compartment of the device. A live/dead assay was performed after 3 days of continuous TMZ perfusion to assess the effect of the therapeutic compound on cancer cells. B) Representative images showing bright-field (BF in Grey), DRAQ7 (Magenta, indicating dead cells), and Calcein (Green, indicating live cells) staining. The scale bar represents 50 µm. C) The fold increment of DRAQ7+ cells was calculated with the corresponding untreated (Sham) group as a reference. Results indicate that cancer cells in the perivascular region are more resistant compared to U87 cells found in the peripheral space or cultured in static hydrogels (Plate 3D). These results were obtained from image analysis of at least 6 ($n \geq 6$) biological replicates from $N = 2$ independent experiments and are expressed as mean ± SEM. Statistical significance was determined using the Brown-Forsythe and Welch ANOVA test, denoted as ns ($p > 0.05$) and *** ($0.0001 < p < 0.001$).

practical challenges. A notable example involves the work of Jordan Miller and colleagues, where the integration of microfluidic hydrogels into pre-assembled chambers made of 3D-printed (FDM) materials, along with shared G-Code, aimed to enhance affordability and accessibility.[60] However, the extended assembly process over three days poses a substantial challenge, impeding the seamless integration of these technologies into routine laboratory practices. Moreover, the resultant bulky structure, connected with screws and bolts, introduces usability challenges that could hinder the widespread adoption of these technologies. This complexity in assembly not only demands an extended period but also may deter users less familiar with intricate 3D-printed structures. As the field advances, addressing these usability challenges becomes relevant for translating these innovative methods from specialized laboratories to broader scientific communities.

Our biofabrication approach enables recreating the vascularized microenvironment of living tissues in a rapid and reproducible way, incorporating tissue-specific endothelial cells within a perfusable hydrogel. We combined SLA printing and extrusion bioprinting to create a streamlined fabrication process, addressing critical concerns of time and complexity. The entire biofabrication process takes ≈2 days. It begins with SLA 3D printing

and cleaning of the microfluidic parts (day 1), followed by the assembly of the microfluidic chamber, bioprinting of sacrificial material (Pluronic), and casting of cell-laden hydrogel, and seeding of endothelial cells (day 2). Leveraging commercially available 3D printers and materials, we were able to simultaneously produce up to 30 functional devices incorporating living cells in a single batch. This not only enhances the pace of fabrication but also significantly reduces the overall complexity, making our approach a valid alternative to previous FDM or PDMS-based approaches. In contrast to PDMS-based microfluidic devices, where cells are physically isolated in parallel compartments, our microfluidic hydrogel design allows molecules to diffuse freely as it would occur in traditional 3D culture. Our approach utilizes a sacrificial template created through bioprinting of a sacrificial material (Pluronic) to generate a microfluidic channel within a fibrin hydrogel. This design merges traditional 3D cell culture methods with microfluidic principles to recreate the dynamic tissue microenvironment, including IFF. In our system, the cell culture medium diffuses through the pores of the fibrin hydrogel. The pressure generated by the medium in the vertical inlets simulates intravascular pressure. The differential pressure (Δp) between the microfluidic compartment and the rest of the hydrogel mimics that of vascularized tissues in living organs. Medium added to the vertical inlets flows from regions of higher pressure (intravascular space) into the extravascular (parenchymal) compartment where cells are localized and exit the system through the porous surface on top of the device. Medium is manually removed daily, akin to traditional static 3D models. This design ensures a facile approach to generating continuous fluid flow, providing nutrients and removing waste products, thereby creating pressure and fluid flow gradients described in our computational model and replicating biomechanical principles regulating physiological IFF.

Our study demonstrates that a construct obtained through the synergistic combination of SLA and bioprinting not only offers advantages in terms of ease of fabrication, scalability, and usability but also provides a platform with demonstrated low absorption properties. This was illustrated in our study on TMZ, a standard-of-care treatment for GBM. Traditional PDMS-made devices are known to exhibit significant absorption of TMZ, whereas our GlioFlow3D platform effectively addresses this long-standing issue, showcasing its potential for overcoming challenges associated with traditional PDMS-made OoC models.

To provide a solid proof-of-concept for the integration of SLA 3D printing and bioprinting in generating functional MPS models, our study presents an innovative approach to biofabricating a microfluidic model of GBM. The GlioFlow3D comprises a vascularized microfluidic compartment lined with HBMECs directly interfaced with astrocytes and cancer cells housed in a 3D hydrogel. This strategy offers advantages over traditional PDMS-based models by capturing biomechanical forces that regulate cell and tissue physiology. The design enables precise control of multiple biophysical factors, including intravascular shear stress, pressure, and interstitial flow, within a biomimetic framework that can be tailored to replicate specific tissues or regions, providing a natural substrate for cells to respond to endogenous and exogenous stimuli. Moreover, this transparent and PDMS-free design is particularly relevant for studying neurological functions and assessing neurological therapeutics. Unlike PDMS-based systems, our approach avoids trapping small molecules in silicone scaffolds, allowing for the testing, accurate detection, and microscopic interrogation of small molecules. Compared to traditional OoC designs that often utilize a "sandwich" or "parallel chamber" assembly,[61] wherein cells are physically confined within microfluidic compartments made of rigid materials,[39,8] our hydrogel-based model overcomes these limitations by allowing cells to move and self-organize within a 3D structure.

The dynamic cell-cell interactions facilitated by the 3D scaffold in our model are central to understanding how drugs influence not only individual cells but also how they respond to stimuli mediated by the surrounding tissue microenvironment. This is particularly relevant in the context of highly heterogenic tissue models such as GBM, where cell-cell communication can significantly impact treatment responses and the development of resistance. Specifically, our study demonstrated that the dynamic co-culture conditions established within the GlioFlow3D model promote the migration of individual tumoral cells with self-renewal potential near perivascular space. Interestingly, these cancer cells exhibit a distinct circular (round) morphology and express the self-renewal marker CD133+, a hallmark of GSCs previously associated with cancer cell proliferation, intra-tumor heterogeneity, and drug resistance.[62] In contrast, cancer cells located in the periphery of the device, away from the vasculature, exhibit a branched morphology and do not express CD133, indicating that the relative distance from the vasculature influences the differentiation or retention of cancer cells with self-renewal potential. The observed differential phenotypical distribution of cancer cells under dynamic co-culture conditions in the GlioFlow3D is further supported by testing the response to TMZ. Cancer cells that localize within the perivascular space in the GlioFlow3D model cultured under dynamic conditions demonstrated enhanced resistance to TMZ treatment compared to static conditions after 3 days of treatment. It is worth noting that the doses of TMZ used in the present study are significantly higher than those typically used in clinical settings, ranging from 75 to 200 mg m^{-2},[63] which equates to 27.6–73.6 mg $liter^{-1}$ (or 0.14–0.38 mM) for an average patient weighing 70 kg and measuring 1,70 m tall. While considerably higher than clinical doses, such a high concentration of chemotherapy falls within the range reported in several in vitro studies.[64] One reason for using high doses of therapeutics in vitro research is that GBM cells are notoriously prone to acquiring a resistant phenotype in vitro.[65] Interestingly, when tested within the dynamic microenvironment of the GlioFlow3D model, we observed a significant variation in cancer cell morphology and sensitivity to the TMZ. Cancer cells in the perivascular region, characterized by circular/round morphology and CD133 expression, exhibited notably higher resistance to treatment compared to cells in static conditions. This increased resistance was not observed in cancer cells located far from the vascular compartment, where IFF was low. These findings highlight the efficacy of our method and model in accurately reproducing the complex dynamics of cell-cell interactions that regulate tissue and organ-level functions, including the protective role of the BBB in brain tumors. Importantly, by simulating intravenous injections, our GlioFlow3D provides a more accurate representation of drug dynamics that cannot be achieved with 3D models lacking vascular perfusion, enabling researchers to investigate how different resident cell types or circulating drugs interact with the vascular

wall, navigate the tissue microenvironment, and reach the target site. The endogenous gradients of IFF within the hydrogel may enable the study of localized drug effects,[66–68] mirroring the in vivo scenario where drugs may exhibit differential impacts across tissue regions. The IFF dynamics contribute to a more realistic simulation of how drugs disperse and interact with cells within the tumor mass, providing crucial insights into drug penetration and distribution.

GBM is infamous for its inter and intra-tumoral heterogeneity and complex niches which play a critical role in therapy resistance, often via GSCs-mediated self-renewal.[69] This rapid prototyping approach stands as a promising platform for developing a personalized tumor model for the exploration of therapy options tailored for individual patients or specific tumors. Notably, our methodology allows for a comprehensive exploration of the mechanisms underlying drug resistance, particularly within the context of the tissue microenvironment in GBM. While our study presents an innovative approach to fabricating vascularized MPSs, it is essential to acknowledge certain limitations of the current study. First, the selection of cell types employed in our model reflects a compromise between availability, ease of maintenance, and the aim to recapitulate key interactions within the tumor microenvironment. Future studies could explore the integration of additional cell types such as microglia and pericytes to enhance the complexity and physiological relevance of the model. Additionally, the exclusive use of fibrin in our hydrogel formulation, while providing a supportive matrix, may not fully capture the diverse composition of the brain extracellular matrix. To this point it is worth noting that our approach includes a coating of vascular channel with specific ECM, however, exploring other hydrogel materials with a closer mimicry of the brain's native environment, such as hyaluronic acid-based blends, could offer improved physiological relevance. Lastly, future studies should focus on integrating patient-derived cells to enhance the physiological relevance and predictive power of our biofabricated model. For example, the aggressive loss of vascular integrity observed in our research work is likely the result of the specific cell line (U87), which is known for rapidly causing edema in mice but does not represent the general behavior of GBM cancer cells that do not always cause vascular edema.[70] Additionally, the present study reports results obtained with primary HBMECs obtained from commercial vendors that are known to develop a relatively low barrier function when compared to freshly isolated or induced pluripotent stem cells (iPSc)-derived cells.[39] Future iterations of this model will include the combined use of iPSc-derived and patient-derived cells to better capture the diverse biological behaviors and interactions present in human tumors, leading to more relevant and translatable findings for clinical applications.[70,71] These considerations open avenues for future refinement, ensuring that our model continues to evolve toward an even more faithful representation of the complex dynamics of GBM in a physiologically relevant setting.

4. Conclusion

This study introduces a novel approach for biofabricating microfluidic models that harness human cell self-assembly properties into perf-usable 3D microtissues, showcasing tissue-level functionality in a PDMS-free system. The integration of SLA 3D printing and bioprinting in our method, exemplified by the innovative GlioFlow3D model, demonstrates a robust proof-of-concept for generating effective and functional MPS models tailored for GBM. Moreover, the high throughput and customizable design of our approach facilitate the future development of a personalized GBM model accommodating its intra/inter-tumoral heterogeneity. The implications of our work extend to offering new insights into complex human pathologies, with potentially transformative implications for future therapeutic strategies.

5. Experimental Section

Microfabrication of 3D Printed Chamber: The SLA scaffold was designed using AutoCAD software and printed at the 1819 Innovation Hub, University of Cincinnati combining industrial SLA printing (Formlabs) and commercially available resin (Grey Resin V5, Formlabs). The outer dimension of the chip is 50 mm (length) by 30 mm (width) by 12 mm (height) which adequately accommodates the 3 mL of hydrogel and cell culture media. Upon completion of the printing process, the support material was removed. Further quality control of the printed parts was performed using ethanol to check whether the inlets were functional. The printed parts were submerged in 99.5% isopropanol (I-MAX) and left overnight at room temperature to allow sufficient time for the leaching of compounds to isopropanol. The next day the resin parts were removed from isopropanol and left at 60 °C overnight. To accommodate the traditional imaging technique with confocal and fluorescent microscopy, we used a microscope slide coverslip made of glass with a thickness of 0.15 mm (Polysciences, Inc.; #23999-1). Fast-curing silicone (QSIL 216, Base and curing agent mix ratio 10:1) was used to seal the space between the glass slide and the 3D-printed parts. 40–60 min of incubation at 60 °C temperature was required to complete the curing process of the sealant agent. To functionalize the inner chamber of our device we used 3-Aminopropyl trimethoxysilane (APTMES, Sigma-Aldrich; #281 778) diluted in absolute ethanol (Fisher Bioreagents) at the final concentration of 5% v/v. The microfluidic chambers were incubated for 15 min in 5% APTES and then washed twice with ethanol to remove APTES residue. Each washing was followed by 2 min incubation in ethanol to ensure the removal of any APTES residual. Resin parts were then incubated at 60 °C overnight to complete the activation step.

Surface Coating and Bioprinting of Sacrificial Templates: To enhance the stability of our construct, we adopted a well-known strategy consisting of pre-coating the cell culture surface with collagen I before casting a hydrogel solution.[72] Collagen type 1 from rat tail (Sigma; C3867) solution was prepared by 1:20 dilution of the stock solution (3 mg mL^{-1}) in HBSS (Sigma; #H6648-1L). 3 mL of coating solution was put in each microfabricated device and incubated for 45 min at 37 °C. Each device was then air-dried in the biosafety cabinet before printing the sacrificial bio ink used to generate the microchannel. The microchannel was designed in AutoCAD and G-code was generated using Ultimaker Cura 4.1.0. A channel of 1 mm diameter was printed using extrusion-based printing (BIO X). Due to its sacrificial nature and printability at room temperature, Pluronic F-127 (35%; Sigma; CAS#9003-11-6) was used as the sacrificial material of choice to generate the microchannel.[73,74] After printing the channel, an air plasma treatment for (45 s) in each chip was employed to sterilize and enhance the adhesion of the fibrin gel.

Casting Cell-Laden Hydrogel and Endothelial Cell Seeding: The sacrificial template was covered with fibrin hydrogel. To this end, fibrinogen (Millipore; 34 157) and thrombin (Sigma; #T4648) were used at the final concentration of 4 mg mL^{-1} and 1 U mL^{-1}, respectively to obtain fibrin gel. Importantly, thrombin was added right before casting the gel over the bioprinted channel to avoid unwanted crosslinking. U87 cells (Angio-proteomic; #cAP-0044 or #cAP-0044RFP) were culture in StableCell DMEM-high glucose (SIGMA; #D0819-500ML) with 10% fetal bovine serum (gibco; REF #A31604-01), 1% sodium pyruvate (Sigma; CAS#113-24-6), 1% MEM amino acid (Sigma), and 0.1% gentamicin (EMO Millipore

Corp; #345 815). To prepare the cell-laden fibrin gel, U87 cells (300 k mL^{-1}) were mixed with repeat pipetting to ensure a homogenous distribution of cells in the hydrogel. Cell-laden fibrin gel (3 mL) was cast in each chip and incubated for 45 min at 37 °C to complete gel polymerization. After incubation, 1 mL of medium was added on top of the gel to continue the culture of cells in fibrin. In the case of astrocytes (Science Cell, #1800), 200k mL^{-1} cells were seeded. The endothelial cell seeding was done after 1 day post-seeding of U87-loaded fibrin. The Pluronic channel was washed with a cold cell culture medium 3 times to remove the Pluronic residue forming a hollow channel. Then the microfluidic channel was coated with a mix of Matrigel (1:50 dilution, 8–12 mg mL, Cultrex, #3445-005-01) and collagen type 1 to create the base membrane for HBMECs (ANGIO-PROTEOMIE; #cAP-0002 or #cAP-0002VE-CADGFP) cells. The endothelial cell basal medium 2 (EGM2, PromoCell; #C-22211) with supplements provided by the vendor was used. The HBMECs were seeded at 2 million/mL concentration. To ensure the channel was populated with endothelial cells on all sides, cells were seeded twice. The devices were kept upside down for 45 min to let the cells attach to the top of the channel interfacing fibrin gel. The residue of the medium and cells was removed, then cells were seeded again keeping devices upright. Each time 150 µL cell suspension was used. All cells were seeded at P6 unless mentioned otherwise. All the reagents were diluted in HBSS without calcium chloride and magnesium sulfate.

Cytocompatibility Testing of 3D Printed Material: Before any experiment, the 3D printed parts were sprayed with isopropanol and left to dry under the UV light for 20 min to reduce the risk of contamination. We subsequently tested the cytocompatibility of the 3D-printed resin material following isopropanol cleaning. The treatment durations varied to determine the optimal incubation time required to suppress potential residual cytotoxicity. Specifically, the treatment times were: no treatment, 30 min, 1 h, 3 h, and overnight. After the isopropanol treatment, the 3D printed parts were submerged in a sterile endothelial cell culture medium (EGM2) and incubated overnight at 37 °C to generate the conditioned medium. The next day, the 3D-printed parts were removed, and the conditioned medium was stored at 4 °C. To assess the potential cytotoxic effects of the conditioned medium, (HBMECs were cultured in 24-well plates. The cells were incubated with the conditioned medium for 3 days post-seeding. Cell viability was evaluated using a live/dead assay. Specifically, cells were stained with HOECHST 33 342 (1 µL mL^{-1} working solution from a 10 mg mL^{-1} stock, Thermo Fisher Scientific; #H3570), DRAQ7 (1:100 working solution from a 0.3 mM stock, Cell Signaling Technology; #7406), and Calcein (1 µL mL^{-1} working solution from a 2.5 mg mL^{-1} stock, Invitrogen; C3100MP), and then imaged using an Olympus fluorescence microscope.

Absorption Test: To characterize the absorption properties of the 3D-printed SLA scaffold compared to traditional PDMS-based devices, we employed two different approaches using Rho123 (Invitrogen; #R302) and TMZ (Sigma-Aldrich; #PHR1437). PDMS devices fabricated from SYLGARD (SYLGARD TM 184 Silicone Elastomer Kit; Dow; #0 401 9862) as previously described elsewhere[8,75] served as the reference material. For Rho123 detection, devices made from either PDMS or SLA resin were perfused with Rho123 and subsequently incubated overnight at room temperature while shielded from light. The next day, the Rho123 solution was removed, and each device underwent thorough washing with water three times, with each wash lasting 5 min. Following washing, we used ImageJ for image acquisition and fluorescent signal analysis to estimate the relative amount of Rho123 remaining trapped in both PDMS and 3D-printed SLA resin. Devices that were not exposed to Rho123 were utilized to establish baseline measurements by assessing the natural autofluorescence of untreated materials. The baseline was subtracted from the results. To evaluate the absorption of TMZ, both PDMS and SLA resin devices were incubated at room temperature with a solution of TMZ (12 mM) in ultrapure water (Sigma, 900682-1L) for 1 h. Subsequently, the collected solution underwent analysis via mass spectrometry to determine the relative abundance of TMZ absorbed by each type of device.

Computational Modelling of Interstitial Fluid Flow: Numerical analysis was performed to characterize the IFF pattern corresponding to the established pressure field in the vascular channel and within the porous hydrogel. The IFF velocity, **v**, depends on the permeability and porosity of the hydrogel as follows:

$$\mathrm{v} = -\frac{k}{\mu\epsilon} grad\,(p) \tag{1}$$

where k is the permeability, μ is the dynamic viscosity of the culture medium (0.00069 Pa.s) and ϵ is the porosity. The porosity of the gel and its permeability were taken from the literature according to the nature of the hydrogel and its composition. The permeability value of 10^{-13} m^2 and a porosity of 0.71 have been used according to a previously published article.[35] To model the porous membrane and the endothelium permeability two convective-type boundary conditions have been adopted:

$$\mathrm{q}_c = h_c\ (p_{sup} - p_0)\,\mathrm{n} \tag{2}$$

where $\mathbf{q}_c$ is the convective flow, h_c is the convection coefficient ($\frac{m}{Pa.\ s}$). For the endothelium, p_{sup} is the pressure at the external surface of the endothelium and p_0 *is* the pressure within the vessel. For the porous membrane p_{sup} is the pressure at the internal surface of the membrane and p_0 *is* the atmospheric pressure assumed here as the reference pressure.

Three different values of h_c were tested for the porous membrane to study how this impacts the established pressure gradient within the hydrogel. The open-source software CAST3M (http://www-cast3m.cea.fr/) has been used to perform the numerical simulations. Post-processing was carried out in ParaView 5.11.1 to visualize the results. The approach used here for this in silico study can be further extended to model the presence of the various cell populations, cell proliferation, and nutrient diffusion as shown by Sciume et al. in different contexts.[76–78]

Cell Viability Assay: The cell viability assay was performed after 3 and 5 days of cell culture. HOECHST, and DRAQ7 were used as staining agents for nuclei and dead cells respectively. 1 mL of staining solution was pipetted on top of the fibrin gel while 150 µL of staining solution was injected to stain the cells in the channel. The sample was incubated for 45–60 min. at 37 °C and washed with fresh cell culture medium twice before imaging. All reagents were diluted in a cell culture medium.

Vascular Permeability: The vascular leakage was tested using dextran blue, 3 kDa (Thermo Fisher Scientific; D7132), or Albumin-Red (Invitrogen; #A23017) as fluid probes. WGA647 (Invitrogen; #W32466) was used to stain the cytoskeleton of cells highlighting the endothelial wall. For dextran, the 1: 100 dilution was made in an endothelial cell culture medium to bring the final dilution of 0.1 mg mL^{-1}. Similarly, for WGA 1:200 dilution was made to bring the concentration down to 5 ng mL^{-1}. About 150 µL of medium containing dextran and WGA was perfused through the channel, and then imaging was performed immediately (t0) and 1 h (t1h) later. The signal intensity of fluorescent molecules was measured using Image J.

To calculate the pApp, the following formula was used as previously done by others[33,79]:

$$\mathrm{pApp} = \frac{Vgel}{Avessel} * \frac{Cgel}{C} * \frac{1}{t} \tag{3}$$

where V_{gel} is the volume of the gel which is 3 mL (3 cm^{-3}), A_{vessel} is the area of the vessel that is in contact with the hydrogel, which is 0.47 cm^2, t is the time period (which is 1 h) and C_{gel} is the concentration of dextran blue or Albumin-Red in the gel. C_{gel} is calculated as:

$$= \frac{C\nu 1}{C\nu 2} * Cg2 \tag{4}$$

where C_{v1} and C_{v2} are signal intensities produced by the fluorescent compounds within the vessel at t0 and t1h respectively. C_{g2} is the signal intensity produced by the fluorescent compounds in the gel at t1h.

Similarly, C is the signal intensity in a vessel, which is calculated as follows:

$$C = C_{v1} - C_{g1} \tag{5}$$

where C_{g1} is the signal intensity produced by the dextran blue or Albumin-Red in the gel at t0.

Quantification of Cytokines and Metalloproteases: The medium was collected from the top surface of the fibrin gel after 6 days in co-culture. The medium was refreshed 24 h before collection. The collected medium was stored at −80 °C before use. Pre-labeled kits for the desired cytokines were used for the Luminex assay.

Fixation and Immunostaining: Samples were fixed in 4% Paraformaldehyde (PFA, Boston Bioproducts, Inc.; #BM-155). 1 mL of 4% was added to the top of the gel, 200 µL through the channel, and incubated for 15 min at room temperature. After the incubation period, both gel and channel were washed with HBSS twice. The fresh HBSS was added and stored in 4c. Fixed samples were permeabilized and blocked using 0.1% Triton (Sigma; #X100) and 2% Blocker BSA (Thermo Scientific; #37 525) respectively. The samples were incubated for 30 min at room temperature with the solution and washed with fresh HBSS. Following the permeabilization and blocking steps, samples were stained with primary antibodies. Ve-Catherine (primary-Invitrogen; PA5-19612, host-Rabbit and secondary-Goat anti-rabbit Alexa Fluro 488; Invitrogen; A32731, both 1:200 dilution) and Anti- hCD31 (PCAM-1) (primary-Novus Biologicals; #AF806, host-sheep and secondary-Donkey anti-sheep Tx red; Sigma; #SAB3700726, both 1:200 dilution) for staining endothelial tight junction were used. anti-cd133 (prominin-1) (primary-Millipore Sigma; #MAB4399-I, host-mouse and secondary-Goat anti-mouse Alexa Fluro 488; Invitrogen; #A32723, both 1:200 dilution) was used to stain the cd133+ cells. Similarly, HOECHST 33 342 to stain nuclei and Phalloidin-Atto 647N (1:1000 dilution, BioReagent; #65906-10NMOL) to stain cytoskeleton was used. For both primary and secondary staining, 1 mL of staining solution in gel and 200 µL inside the channel was used. All the staining reagents were diluted in HBSS. Overnight incubation at 4c was done with primary antibodies. For secondary antibodies, at least 2 h. of incubation away from light was done. For both primary and secondary staining, all samples were washed twice with 5 min wait time in each wash to remove any unbound antibodies. The stained samples mounted in HBSS were stable in 4c for 1–3 weeks during the imaging period. Olympus Fluorescent microscope was used for imaging.

Cell Morphology and Shape Index: The cell morphology was analyzed using Image J and the free plugin named "BioVoxxel _Toolbox". The plugin generates a set of data reporting the shape of each cell using a shape index. The shape index ranges between 0 (elongated objects) and 1 (perfectly round objects).

PECAM1 Signal Measurement: Following fixation with PFA, samples were stained for the PECAM1 marker. Fluorescence images were then processed using ImageJ software. To quantify the length of tight junctions, the images were analyzed with the "Analyze Skeleton (2D/3D)" tool in ImageJ, which provided numerical measurements of the junction lengths.

Temozolomide Preparation and Treatment: TMZ (Sigma-Aldrich; #PHR1437) was used as the therapeutic reagent of choice to assess the response of GBM cancer cells (U87) cultured in the GlioFlow3D model. TMZ media was prepared by dissolving TMZ powder (2.5 mg mL^{-1}) in a full endothelial cell culture medium. Additionally, 0.1% dimethyl sulfoxide (DMSO; ATCC) was added to the medium, which was left on a shaker at 37 °C overnight to facilitate the dissolution of the powder. The next day, the medium was filtered using a 0.2 µm filter to ensure sterility before use. As described in the results section, GlioFlow3D systems were cultured for 2 days under dynamic conditions without TMZ. The TMZ treatment commenced on day 3 of culture. To ensure a continuous supply of TMZ through the vascular channel, we connected the devices to a syringe pump using tubing (Cole-Parmer, #EW9566601) and Luer lock connectors (AIEX; #B13245). The pump was set at ≈5 cm above the microfluidic devices to maintain constant pressure and flow parameters. The treatment lasted for 3 days, with a total volume of ≈1.5 mL of media per day being perfused into the hydrogel, ensuring effective and consistent therapeutic exposure throughout the treatment duration. Considering the small molecular size of TMZ and previous studies demonstrating the rapid penetration of TMZ across the BBB,[80,81] it is likely that the concentration of TMZ in the hydrogel will be similar to that in the perfusion channel within a short period. After 3 days of continuous treatment, cell viability was assessed via live/dead staining using DRAQ7 (for nuclei of dead cells), Calcein (for living cells), and HOECHST 33 342 (for all cell nuclei).

Statistical Analysis: In all experiments, each device containing cells was considered an independent biological replicate. For each condition, experiments were performed in at least 2 separate runs. Statistical analysis was performed using the software GraphPad Prism 10. ANOVA or t-test was used to determine the statistical significance where $p > 0.05$ (ns), $0.01 < p < 0.05$ (*), $0.001 < p < 0.01$ (**), $0.0001 < p < 0.001$ (***), $p < 0.0001$ (****). Graphs are represented as average values ± SEM from at least $n = 3$ biological replicates unless indicated otherwise. Detailed statistics are indicated in each figure legend.

Supporting Information

Supporting Information is available from the Wiley Online Library or from the author.

Acknowledgements

This work was supported by the Brain Tumor Center Research Award and the Neurobiology Research Center Research Award at the University of Cincinnati. The authors thank Dr. Larry Sallans for his expert assistance with mass spectrometry (Department of Chemistry, University Cincinnati). Also, the authors like to thank Amanda Rainey (Cincinnati Children's, Bio Imaging and Analysis Facility) for her assistance with confocal imaging and analysis. The authors thank Alyssa Sproles (Cincinnati Children's, Flow Cytometry Facility) for helping the authors with the Luminex assay.

Conflict of Interest

The authors declare no conflict of interest.

Author Contributions

The authors describe their contributions to the work as follows. S.P. performed data curation, investigation, methodology, visualization, wrote, reviewed and edited the original draft. A.P. and D.D. performed investigation. D.P.K. performed conceptualization, funding acquisition, wrote, reviewed and edited the original draft. G.S. performed conceptualization, formal analysis, investigation, software, supervision, visualization, wrote, reviewed and edited the original draft. S.S. performed conceptualization, funding acquisition, methodology, resources, wrote, reviewed and edited the original draft. R.B. performed conceptualization, data curation, formal analysis, funding acquisition, methodology, resources, supervision, visualization, wrote, reviewed and edited the original draft.

Data Availability Statement

The data that support the findings of this study are available from the corresponding author upon reasonable request.

Keywords

3D printing, bioprinting, glioblastoma, microphysiological systems, organ-on-Chip, rapid prototyping

Received: May 20, 2024
Revised: July 10, 2024
Published online:

[1] D. Sun, W. Gao, H. Hu, S. Zhou, *Acta Pharm. Sin. B* **2022**, *12*, 3049.
[2] L. Meigs, *ALTEX* **2018**, 275.
[3] *Cancer Discov* **2023**, *13*, 805.
[4] D. E. Ingber, *Nat. Rev. Genet.* **2022**, *23*, 467.
[5] P. Ng, C. Belgur, S. Barthakur, A. D. Van Der Meer, G. A. Hamilton, R. Barrile, *Curr. Opin. Toxicol.* **2019**, *17*, 1.
[6] M. Kasendra, A. Tovaglieri, A. Sontheimer-Phelps, S. Jalili-Firoozinezhad, A. Bein, A. Chalkiadaki, W. Scholl, C. Zhang, H. Rickner, C. A. Richmond, H. Li, D. T. Breault, D. E. Ingber, *Sci. Rep.* **2018**, *8*, 2871.
[7] M. Kasendra, R. Luc, J. Yin, D. V. Manatakis, G. Kulkarni, C. Lucchesi, J. Sliz, A. Apostolou, L. Sunuwar, J. Obrigewitch, K.-J. Jang, G. A. Hamilton, M. Donowitz, K. Karalis, *eLife* **2020**, *9*, e50135.
[8] A. Jain, R. Barrile, A. Van Der Meer, A. Mammoto, T. Mammoto, K. De Ceunynck, O. Aisiku, M. Otieno, C. Louden, G. Hamilton, R. Flaumenhaft, D. Ingber, *Clin. Pharmacol. Ther.* **2018**, *103*, 332.
[9] K.-J. Jang, M. A. Otieno, J. Ronxhi, H.-K. Lim, L. Ewart, K. R. Kodella, D. B. Petropolis, G. Kulkarni, J. E. Rubins, D. Conegliano, J. Nawroth, D. Simic, W. Lam, M. Singer, E. Barale, B. Singh, M. Sonee, A. J. Streeter, C. Manthey, B. Jones, A. Srivastava, L. C. Andersson, D. Williams, H. Park, R. Barrile, J. Sliz, A. Herland, S. Haney, K. Karalis, D. E. Ingber, et al., *Sci. Transl. Med.* **2019**, *11*, eaax5516.
[10] T. Osaki, S. G. M. Uzel, R. D. Kamm, *Nat. Protoc.* **2020**, *15*, 421.
[11] L. Ewart, A. Apostolou, S. A. Briggs, C. V. Carman, J. T. Chaff, A. R. Heng, S. Jadalannagari, J. Janardhanan, K.-J. Jang, S. R. Joshipura, M. M. Kadam, M. Kanellias, V. J. Kujala, G. Kulkarni, C. Y. Le, C. Lucchesi, D. V. Manatakis, K. K. Maniar, M. E. Quinn, J. S. Ravan, A. C. Rizos, J. F. K. Sauld, J. D. Sliz, W. Tien-Street, D. R. Trinidad, J. Velez, M. Wendell, O. Irrechukwu, P. K. Mahalingaiah, D. E. Ingber, et al., *Commun. Med.* **2022**, *2*, 154.
[12] L. A. Low, D. A. Tagle, *Exp. Biol. Med.* **2017**, *242*, 1573.
[13] A. E. Danku, E.-H. Dulf, C. Braicu, A. Jurj, I. Berindan-Neagoe, *Front. Bioeng. Biotechnol.* **2022**, *10*, 840674.
[14] B. J. van Meer, H. de Vries, K. S. A. Firth, J. van Weerd, L. G. J. Tertoolen, H. B. J. Karperien, P. Jonkheijm, C. Denning, A. P. IJzerman, C. L. Mummery, *Biochem. Biophys. Res. Commun.* **2017**, *482*, 323.
[15] W. A. Banks, N. H. Greig, *Future Med. Chem.* **2019**, *11*, 489.
[16] X. Zhang, L. Li, C. Luo, *Lab Chip* **2016**, *16*, 1757.
[17] S. Grebenyuk, A. R. Abdel Fattah, M. Kumar, B. Toprakhisar, G. Rustandi, A. Vananroye, I. Salmon, C. Verfaillie, M. Grillo, A. Ranga, *Nat. Commun.* **2023**, *14*, 193.
[18] S. Pun, L. C. Haney, R. Barrile, *Micromachines* **2021**, *12*, 1250.
[19] H. Lee, D.-W. Cho, *Lab Chip* **2016**, *16*, 2618.
[20] N. P. Macdonald, J. M. Cabot, P. Smejkal, R. M. Guijt, B. Paull, M. C. Breadmore, *Anal. Chem.* **2017**, *89*, 3858.
[21] A. J. L. Morgan, L. Hidalgo San Jose, W. D. Jamieson, J. M. Wymant, B. Song, P. Stephens, D. A. Barrow, O. K. Castell, *PLoS One* **2016**, *11*, e0152023.
[22] S. Kreß, R. Schaller-Ammann, J. Feiel, J. Priedl, C. Kasper, D. Egger, *Materials* **2020**, *13*, 3011.
[23] O. G. Taylor, J. S. Brzozowski, K. A. Skelding, *Front. Oncol.* **2019**, *9*, 963.
[24] N. A. Charles, E. C. Holland, *Cell Cycle* **2010**, *9*, 3084.
[25] E. Jung, M. Osswald, M. Ratliff, H. Dogan, R. Xie, S. Weil, D. C. Hoffmann, F. T. Kurz, T. Kessler, S. Heiland, A. Von Deimling, F. Sahm, W. Wick, F. Winkler, *Nat. Commun.* **2021**, *12*, 1014.
[26] A. Milovanović, M. Milošević, G. Mladenović, B. Likozar, K. Čolić, N. Mitrović, in *Experimental and Numerical Investigations in Materials Science and Engineering*, Springer International Publishing, Cham, **2019**, pp. 84–95.
[27] E. Kluska, P. Gruda, N. Majca-Nowak, *Trans. Aerosp. Res.* **2018**, *2018*, 69.
[28] A. Tony, I. Badea, C. Yang, Y. Liu, G. Wells, K. Wang, R. Yin, H. Zhang, W. Zhang, *Polymers* **2023**, *15*, 1926.
[29] W. Li, J. Zhou, Y. Xu, *Biomed. Rep.* **2015**, *3*, 617.
[30] E. Sano, C. Mori, N. Matsuoka, Y. Ozaki, K. Yagi, A. Wada, K. Tashima, S. Yamasaki, K. Tanabe, K. Yano, Y. Torisawa, *Micromachines* **2019**, *10*, 793.
[31] V. J. Herbener, T. Burster, A. Goreth, M. Pruss, H. Von Bandemer, T. Baisch, R. Fitzel, M. D. Siegelin, G. Karpel-Massler, K.-M. Debatin, M.-A. Westhoff, H. Strobel, *Biomedicines* **2020**, *8*, 151.
[32] M. Adiraj Iyer, D. T. Eddington, *Lab Chip* **2019**, *19*, 574.
[33] G. S. Offeddu, L. Possenti, J. T. Loessberg-Zahl, P. Zunino, J. Roberts, X. Han, D. Hickman, C. G. Knutson, R. D. Kamm, *Small* **2019**, *15*, 1902393.
[34] N. Namba, Y. Chonan, T. Nunokawa, O. Sampetrean, H. Saya, R. Sudo, *Tissue Eng., Part A* **2021**, *27*, 467.
[35] O. Moreno-Arotzena, J. Meier, C. Del Amo, J. García-Aznar, *Materials* **2015**, *8*, 1636.
[36] S. W. Schneider, T. Ludwig, L. Tatenhorst, S. Braune, H. Oberleithner, V. Senner, W. Paulus, *Acta Neuropathol.* **2004**, *107*, 272.
[37] A. Rodriguez, S. Tatter, W. Debinski, *Pharmaceutics* **2015**, *7*, 175.
[38] W. S. Kamoun, C. D. Ley, C. T. Farrar, A. M. Duyverman, J. Lahdenranta, D. A. Lacorre, T. T. Batchelor, E. Di Tomaso, D. G. Duda, L. L. Munn, D. Fukumura, A. G. Sorensen, R. K. Jain, *J. Clin. Oncol.* **2009**, *27*, 2542.
[39] G. D. Vatine, R. Barrile, M. J. Workman, S. Sances, B. K. Barriga, M. Rahnama, S. Barthakur, M. Kasendra, C. Lucchesi, J. Kerns, N. Wen, W. R. Spivia, Z. Chen, J. Van Eyk, C. N. Svendsen, *Cell Stem Cell* **2019**, *24*, 995.
[40] R. Albulescu, E. Codrici, I. D. Popescu, S. Mihai, L. G. Necula, D. Petrescu, M. Teodoru, C. P. Tanase, *Mediat. Inflamm.* **2013**, *2013*, 1.
[41] H. Wolburg, S. Noell, P. Fallier-Becker, A. F. Mack, K. Wolburg-Buchholz, *Mol. Aspects Med.* **2012**, *33*, 579.
[42] R. Gómez-Oliva, S. Domínguez-García, L. Carrascal, J. Abalos-Martínez, R. Pardillo-Díaz, C. Verástegui, C. Castro, P. Nunez-Abades, N. Geribaldi-Doldán, *Front. Oncol.* **2021**, *10*, 614295.
[43] D. Hambardzumyan, G. Bergers, *Trends Cancer* **2015**, *1*, 252.
[44] M. Ustun, S. Rahmani Dabbagh, I. Ilci, T. Bagci-Onder, S. Tasoglu, *Micromachines* **2021**, *12*, 490.
[45] Y. Xiao, D. Kim, B. Dura, K. Zhang, R. Yan, H. Li, E. Han, J. Ip, P. Zou, J. Liu, A. T. Chen, A. O. Vortmeyer, J. Zhou, R. Fan, *Adv. Sci.* **2019**, *6*, 1801531.
[46] H. Motaln, A. Koren, K. Gruden, Ž. Ramšak, C. Schichor, T. T. Lah, *Oncotarget* **2015**, *6*, 40998.
[47] M. D. Brooks, R. Sengupta, S. C. Snyder, J. B. Rubin, *Curr. Pathobiol. Rep.* **2013**, *1*, 101.
[48] A. Roos, Z. Ding, J. C. Loftus, N. L. Tran, *Front. Oncol.* **2017**, *7*, 120.
[49] M. T. Ngo, J. N. Sarkaria, B. A. C. Harley, *Adv. Sci.* **2022**, *9*, 2201888.
[50] S. Shojaei, J. Basso, M. Amereh, J. Alizadeh, T. Dehesh, S. De Silva Rosa, C. Clark, M. Hassan, M. Tomczyk, L. Cole, G. Hatch, V. Dolinsky, C. Pasco, D. Schibli, S. Dhingra, A. Srivastava, A. Ravandi, R. Vitorino, S. Ghavami, M. Akbari, *BioRxiv* **2022**. https://doi.org/10.1101/2022.10.29.514383
[51] A. L. V. Alves, I. N. F. Gomes, A. C. Carloni, M. N. Rosa, L. S. Da Silva, A. F. Evangelista, R. M. Reis, V. A. O. Silva, *Stem Cell Res. Ther.* **2021**, *12*, 206.
[52] V. Mattei, F. Santilli, S. Martellucci, S. Delle Monache, J. Fabrizi, A. Colapietro, A. Angelucci, C. Festuccia, *Int. J. Mol. Sci.* **2021**, *22*, 3863.
[53] M. Paolillo, S. Comincini, S. Schinelli, *Cancers* **2021**, *13*, 2449.
[54] J. V. Joseph, M. S. Blaavand, T. Daubon, F. Ae. Kruyt, M. K. Thomsen, *Curr. Opin. Pharmacol.* **2021**, *61*, 91.
[55] E. R. Neves, B. A. C. Harley, S. Pedron, *Brain Res. Bull.* **2021**, *174*, 220.
[56] M. A. Chliara, S. Elezoglou, I. Zergioti, *Biosensors* **2022**, *12*, 1135.

[57] M. Rothbauer, C. Eilenberger, S. Spitz, B. E. M. Bachmann, S. R. A. Kratz, E. I. Reihs, R. Windhager, S. Toegel, P. Ertl, *Front. Bioeng. Biotechnol.* **2022**, *10*, 837087.
[58] H.-G. Yi, Y. H. Jeong, Y. Kim, Y.-J. Choi, H. E. Moon, S. H. Park, K. S. Kang, M. Bae, J. Jang, H. Youn, S. H. Paek, D.-W. Cho, *Nat. Biomed. Eng.* **2019**, *3*, 509.
[59] K. A. Homan, D. B. Kolesky, M. A. Skylar-Scott, J. Herrmann, H. Obuobi, A. Moisan, J. A. Lewis, *Sci. Rep.* **2016**, *6*, 34845.
[60] I. S. Kinstlinger, G. A. Calderon, M. K. Royse, A. K. Means, B. Grigoryan, J. S. Miller, *Nat. Protoc.* **2021**, *16*, 3089.
[61] Q. Wu, J. Liu, X. Wang, L. Feng, J. Wu, X. Zhu, W. Wen, X. Gong, *Biomed. Eng. Online* **2020**, *19*, 9.
[62] D. V. Brown, G. Filiz, P. M. Daniel, F. Hollande, S. Dworkin, S. Amiridis, N. Kountouri, W. Ng, A. P. Morokoff, T. Mantamadiotis, *PLoS One* **2017**, *12*, e0172791.
[63] A. S. Karve, J. M. Desai, N. Dave, T. M. Wise-Draper, G. A. Gudelsky, T. N. Phoenix, B. DasGupta, S. Sengupta, D. R. Plas, P. B. Desai, *Cancer Chemother. Pharmacol.* **2022**, *90*, 345.
[64] M. T. C. Poon, M. Bruce, J. E. Simpson, C. J. Hannan, P. M. Brennan, *BMC Cancer* **2021**, *21*, 1240.
[65] M. Witusik-Perkowska, D. J. Jaskólski, P. P. Liberski, J. Szemraj, *Cell. Mol. Neurobiol.* **2022**, *42*, 1005.
[66] C. T. Curley, B. P. Mead, K. Negron, N. Kim, W. J. Garrison, G. W. Miller, K. M. Kingsmore, E. A. Thim, J. Song, J. M. Munson, A. L. Klibanov, J. S. Suk, J. Hanes, R. J. Price, *Sci. Adv.* **2020**, *6*, eaay1344.
[67] K. M. Kingsmore, A. Vaccari, D. Abler, S. X. Cui, F. H. Epstein, R. C. Rockne, S. T. Acton, J. M. Munson, *APL Bioeng.* **2018**, *2*, 031905.
[68] J. Munson, A. Shieh, *Cancer Manag. Res.* **2014**, 317.
[69] D. Schiffer, L. Annovazzi, C. Casalone, C. Corona, M. Mellai, *Cancers* **2018**, *11*, 5.
[70] A. F. Haddad, J. S. Young, D. Amara, M. S. Berger, D. R. Raleigh, M. K. Aghi, N. A. Butowski, *Neuro-Oncol. Adv.* **2021**, *3*, vdab100.
[71] K. Boylin, G. V. Aquino, M. Purdon, K. Abedi, M. Kasendra, R. Barrile, *Biofabrication* **2024**, *16*, 032007.
[72] V. Reyhani, P. Seddigh, B. Guss, R. Gustafsson, L. Rask, K. Rubin, *Biochem. J.* **2014**, *462*, 113.
[73] S. Liu, T. Wang, S. Li, X. Wang, *Polymers* **2022**, *14*, 2182.
[74] R. Suntornnond, E. Y. S. Tan, J. An, C. K. Chua, *Sci. Rep.* **2017**, *7*, 16902.
[75] A. Jain, A. D. van der Meer, A.-L. Papa, R. Barrile, A. Lai, B. L. Schlechter, M. A. Otieno, C. S. Louden, G. A. Hamilton, A. D. Michelson, A. L. Frelinger, D. E. Ingber, *Biomed. Microdevices* **2016**, *18*, 73.
[76] G. Sciumè, W. G. Gray, F. Hussain, M. Ferrari, P. Decuzzi, B. A. Schrefler, *Comput. Mech.* **2014**, *53*, 465.
[77] G. Sciumè, S. Shelton, W. G. Gray, C. T. Miller, F. Hussain, M. Ferrari, P. Decuzzi, B. A. Schrefler, *New J. Phys.* **2013**, *15*, 015005.
[78] G. Sciumè, R. Santagiuliana, M. Ferrari, P. Decuzzi, B. A. Schrefler, *Phys. Biol.* **2014**, *11*, 065004.
[79] V. Van Duinen, A. Van Den Heuvel, S. J. Trietsch, H. L. Lanz, J. M. Van Gils, A. J. Van Zonneveld, P. Vulto, T. Hankemeier, *Sci. Rep.* **2017**, *7*, 18071.
[80] A. Krajcer, E. Grzywna, J. Lewandowska-Łańcucka, *Biomed. Pharmacother.* **2023**, *165*, 115174.
[81] H.-L. Liu, C.-Y. Huang, J.-Y. Chen, H.-Y. J. Wang, P.-Y. Chen, K.-C. Wei, *PLoS One* **2014**, *9*, e114311.